



the
abdus salam
international centre for theoretical physics

ICTP 40th Anniversary

SMR.1568- 11

SUMMER SCHOOL IN COSMOLOGY AND ASTROPARTICLE PHYSICS

28 June - 10 July 2004

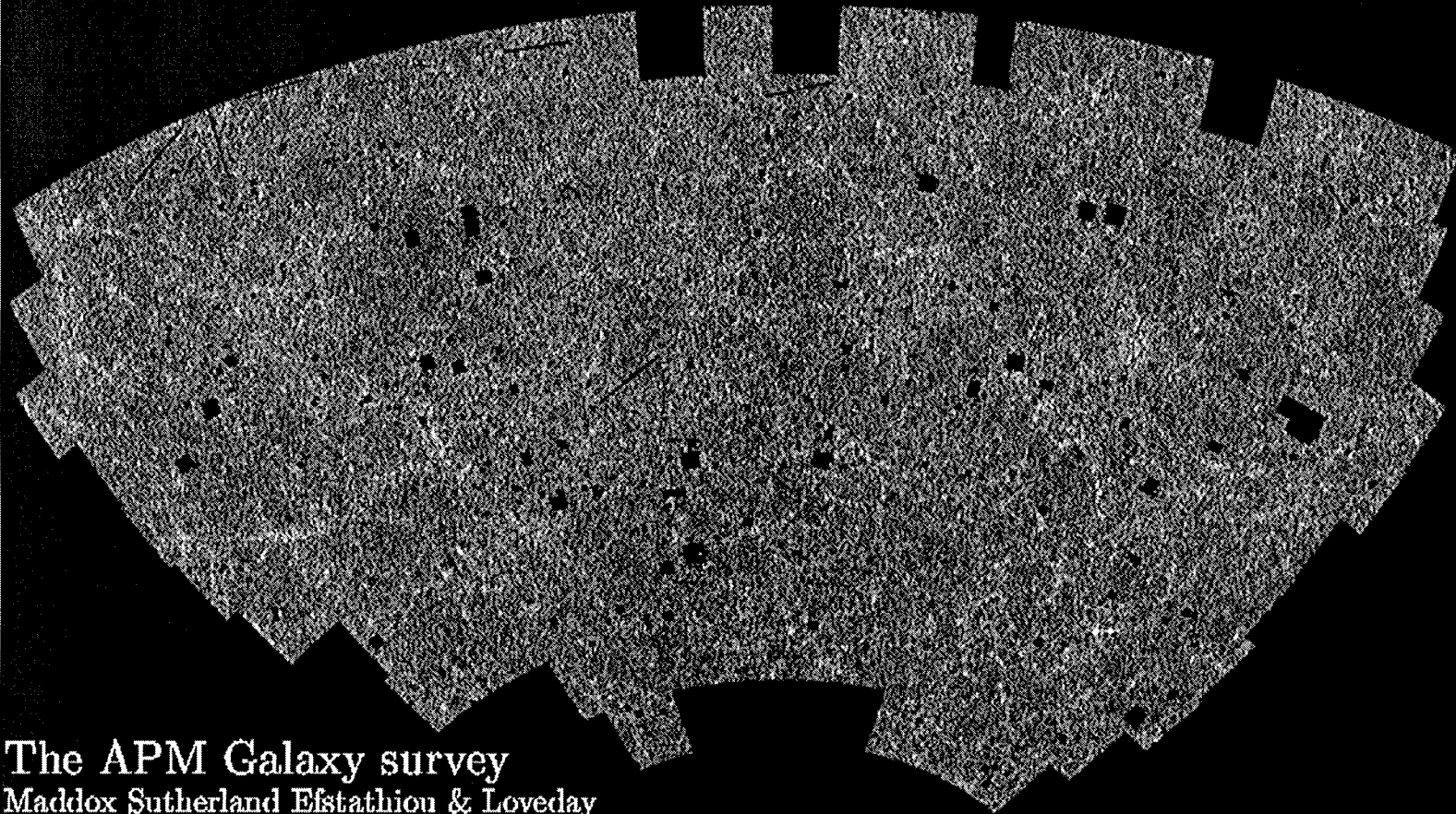
An introduction to CMB anisotropies (V)

**Matias ZALDARRIAGA
Center for Astrophysics
Perkin Laboratory
Harvard University
Cambridge, MA 02138
U.S.A.**

Please note: These are preliminary notes intended for internal distribution only.

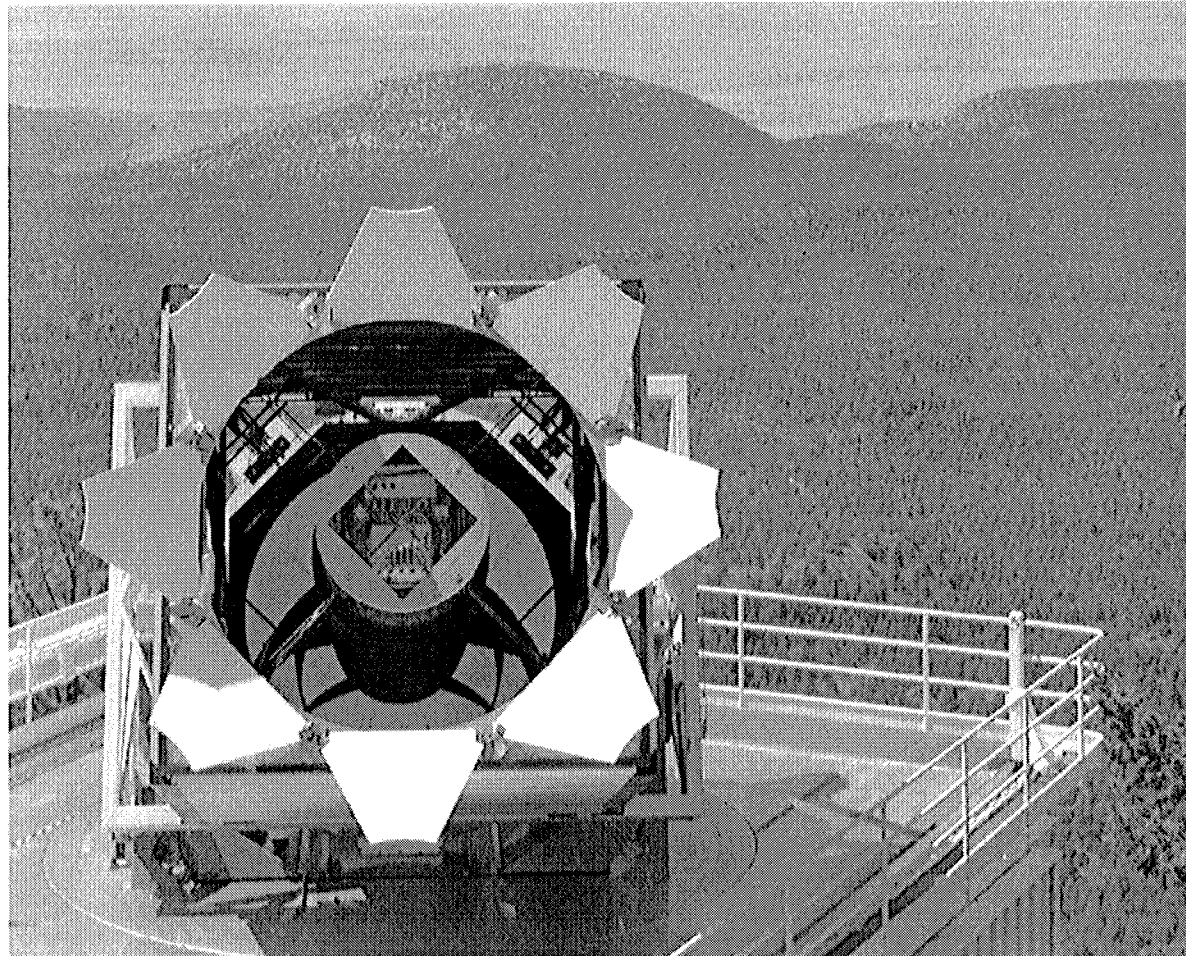
Constraints on parameters:
Combining CMB with other
Probes

The distribution of matter as traced by galaxies

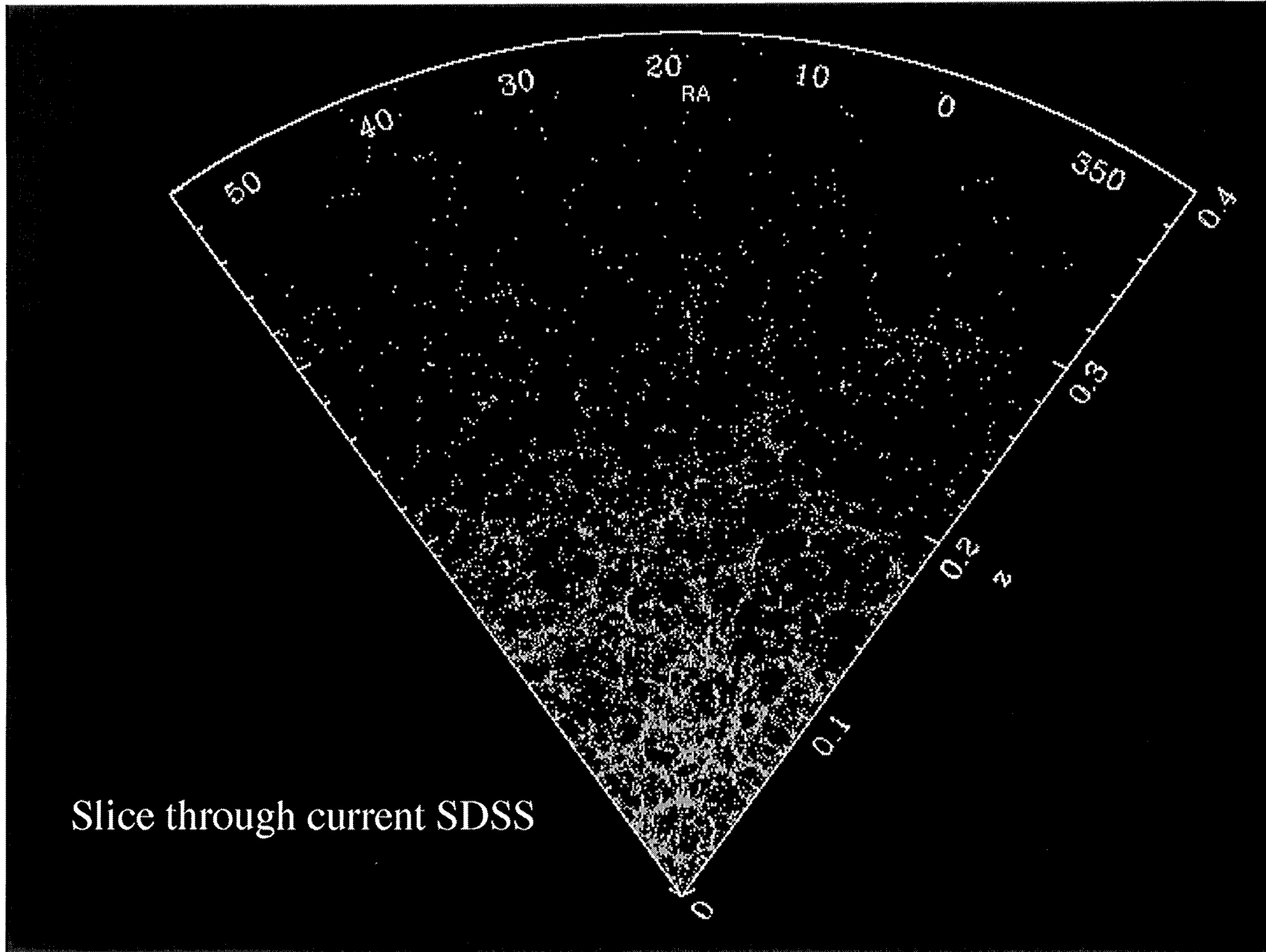


The APM Galaxy survey
Maddox Sutherland Efstathiou & Loveday

The Sloan Digital Sky Survey




1/4 of the Sky in 5 colors, 1 million redshifts



Slice through current SDSS

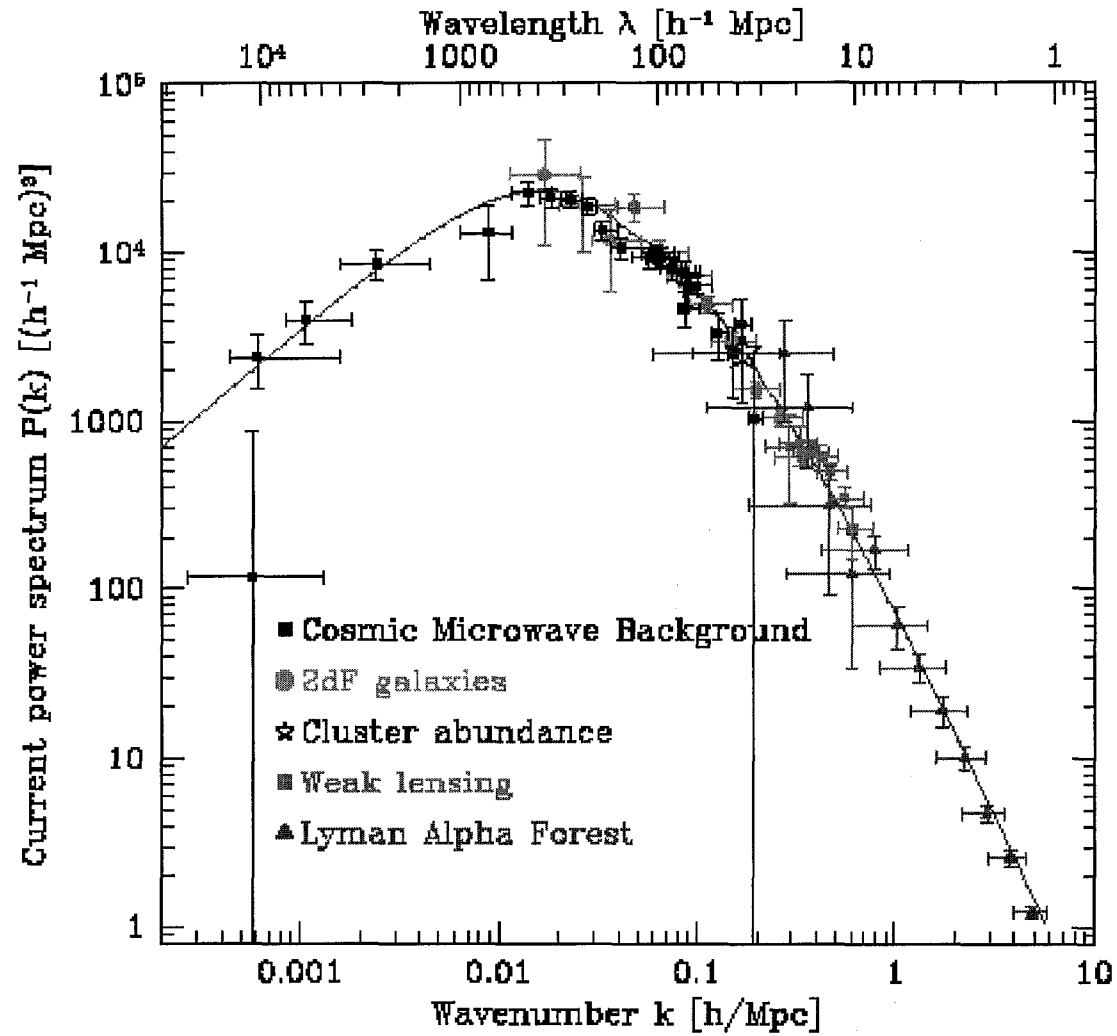
Gravitational Instability

t_1 

$t_2 > t_1$ 

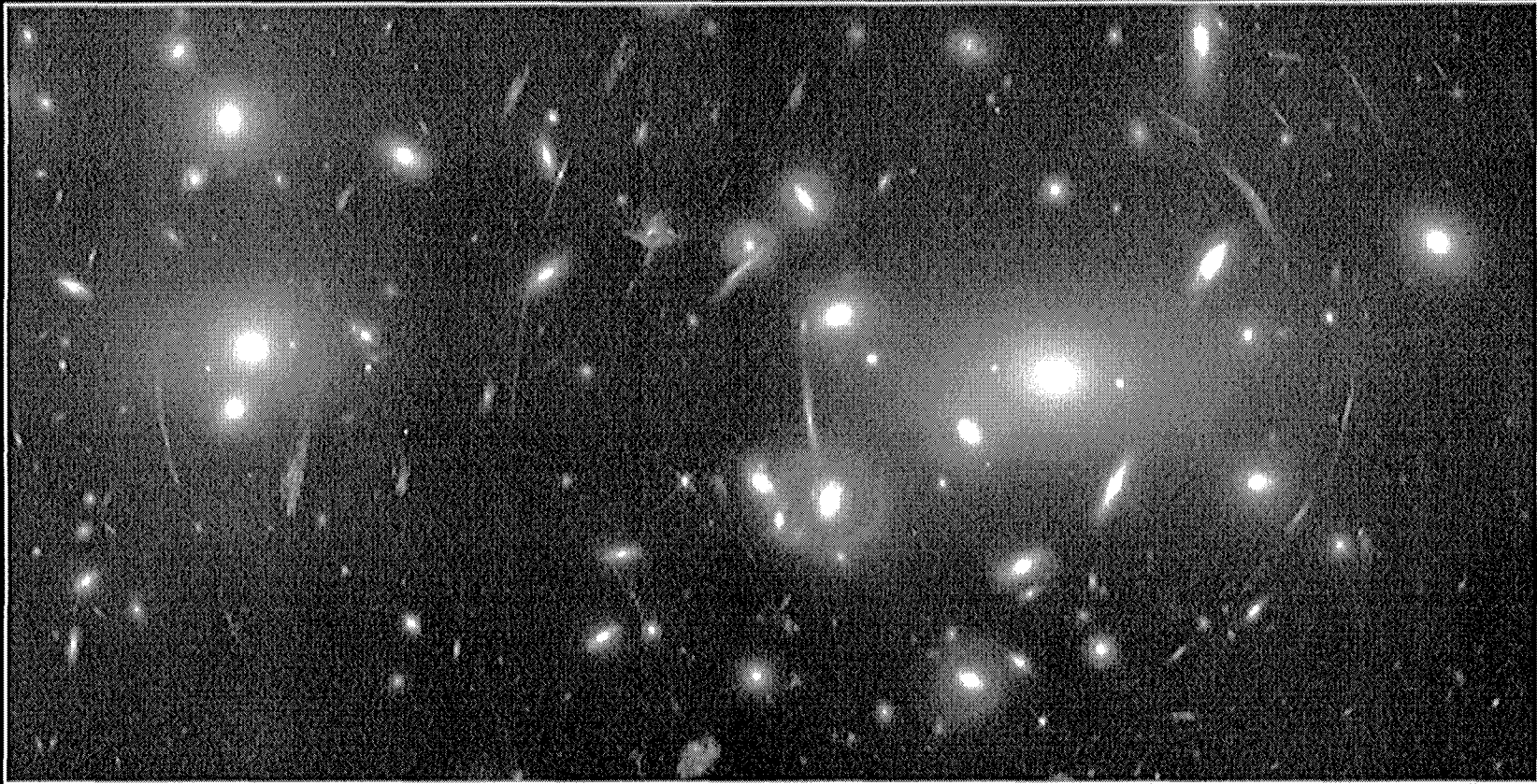
$$t_g \sim (G\rho)^{-1/2}$$

Inferred matter fluctuations at present epoch



Tegmark & MZ

The Gravitational Lensing Effect

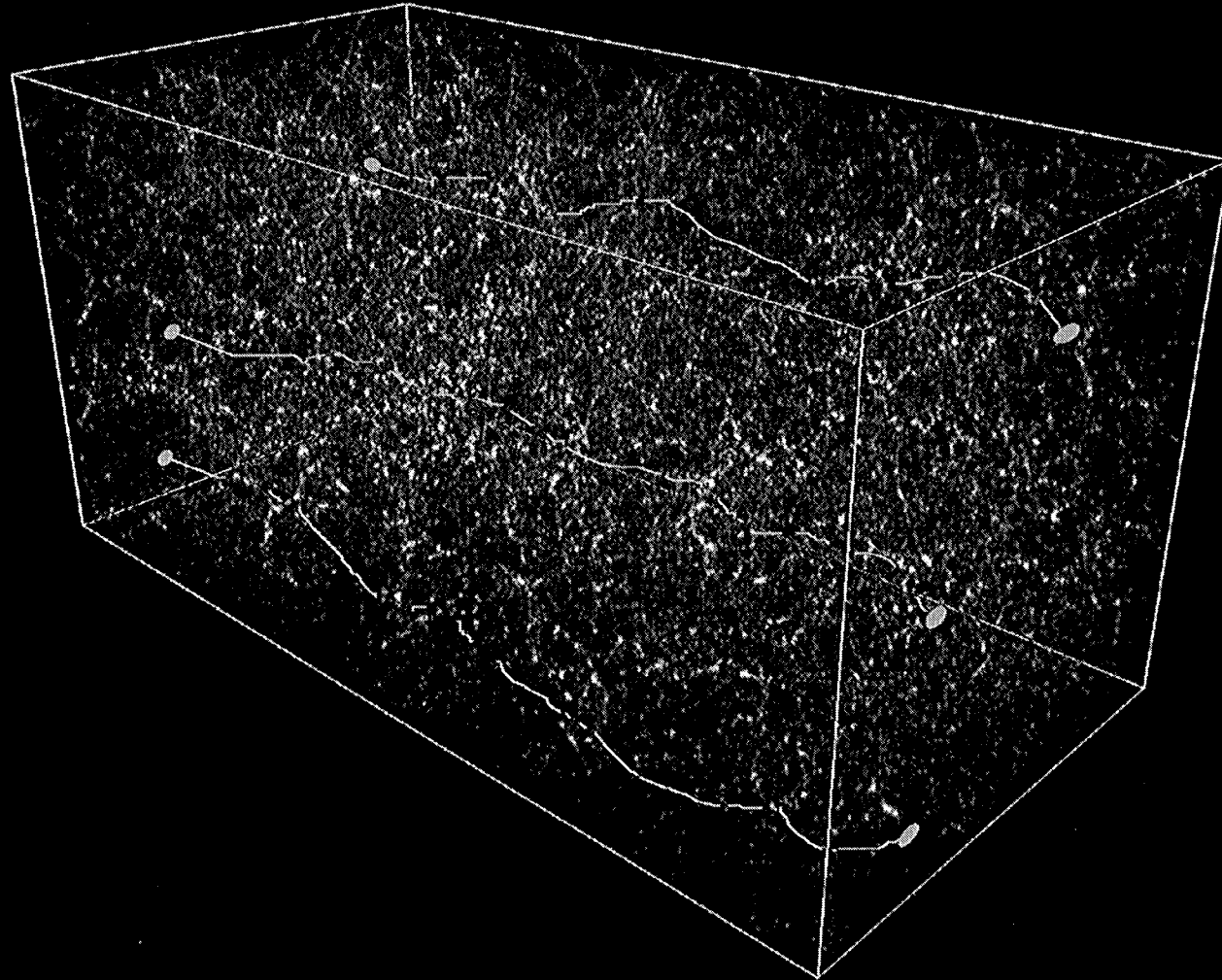


Gravitational Lens in Abell 2218

HST · WFPC2

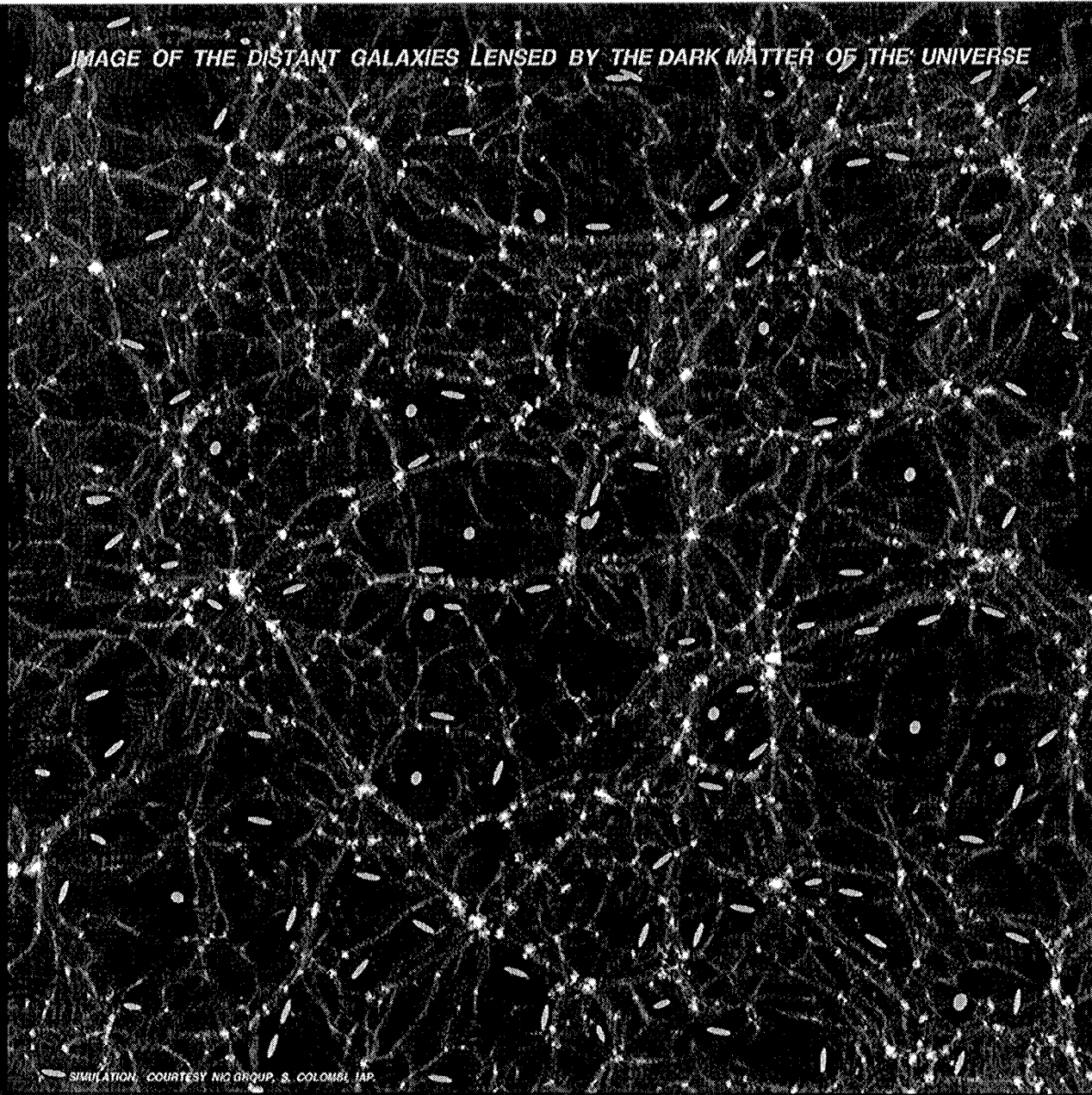
PF95-14 · ST ScI OPO · April 5, 1995 · W. Couch (UNSW), NASA

DEFLECTION OF LIGHT RAYS CROSSING THE UNIVERSE, EMITTED BY DISTANT GALAXIES

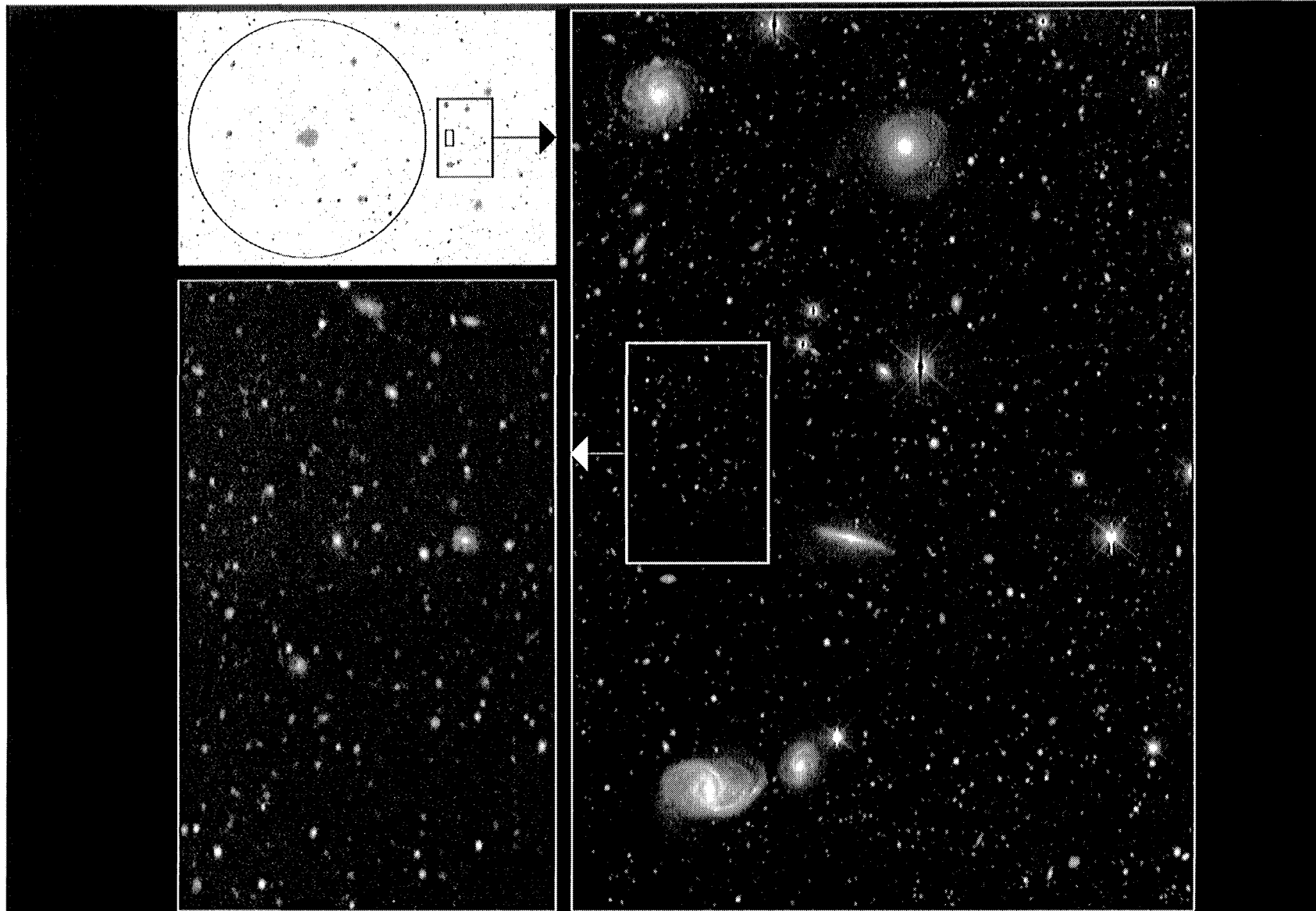


SIMULATION: COURTESY NIC GROUP, S. COLOMBI, IAP.

IMAGE OF THE DISTANT GALAXIES LENSED BY THE DARK MATTER OF THE UNIVERSE



SIMULATION, COURTESY NIJ GROUP, S. COLOMBI, IAP.

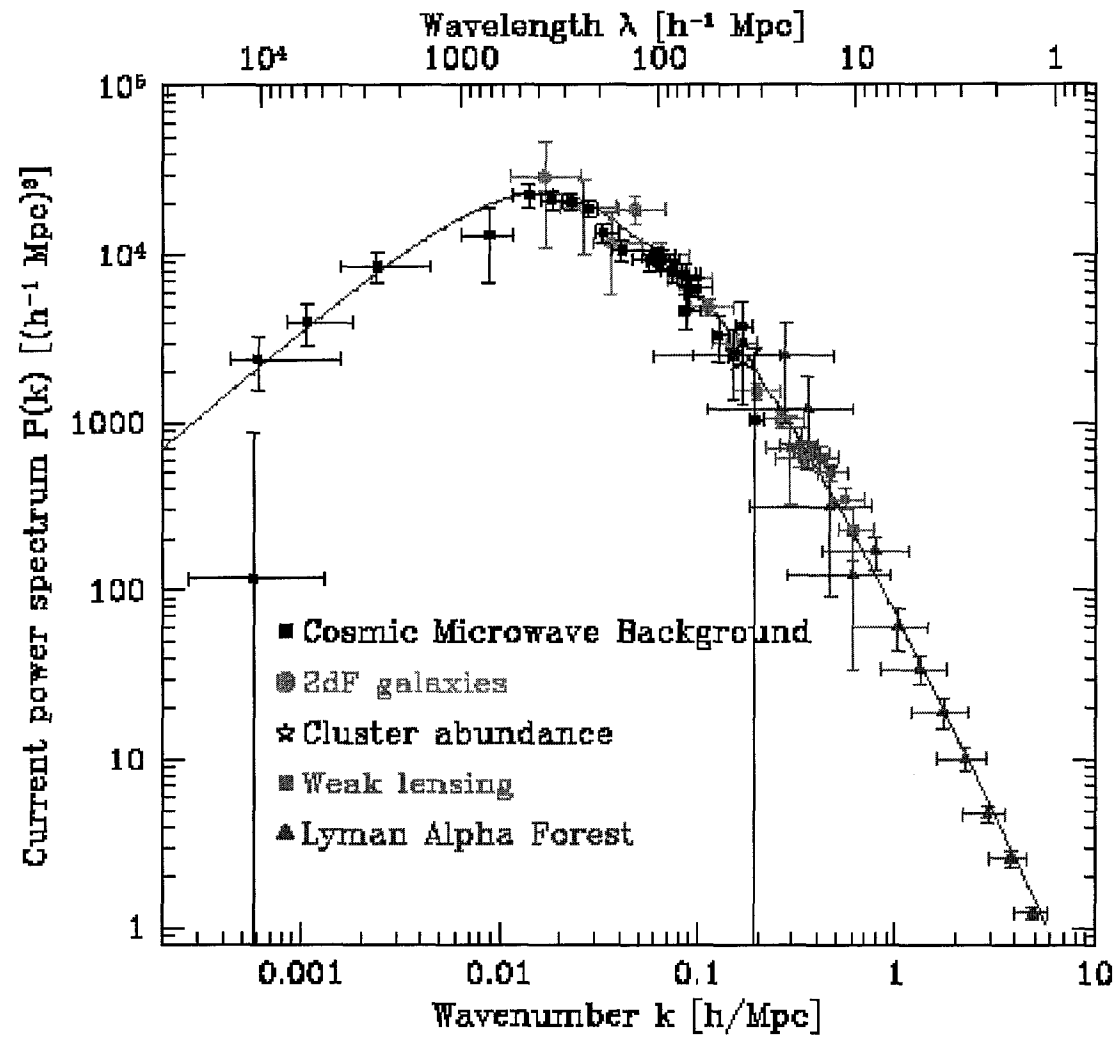


Probing the Universe - Wide-field imaging at CFHT with the CFH12K camera

Images by J.-C. Cullandre (CFHT), © 2000 CFHT



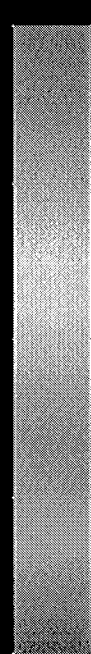
Inferred matter fluctuations at present epoch



Tegmark & MZ

The Lyman alpha forest

$Z = 3$



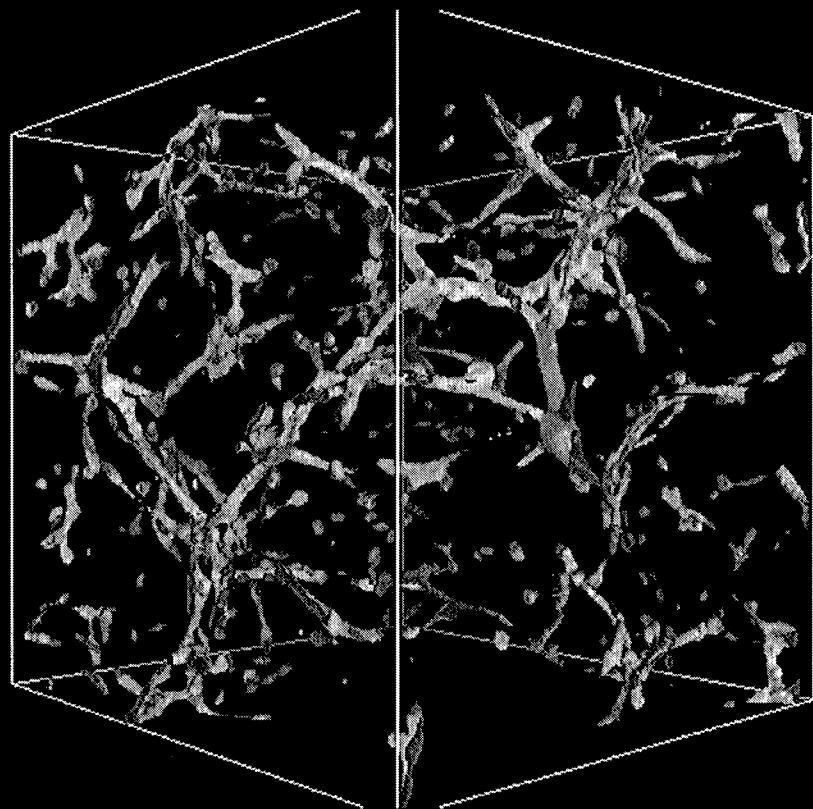
5.0

4.9

4.8

4.6

4.5

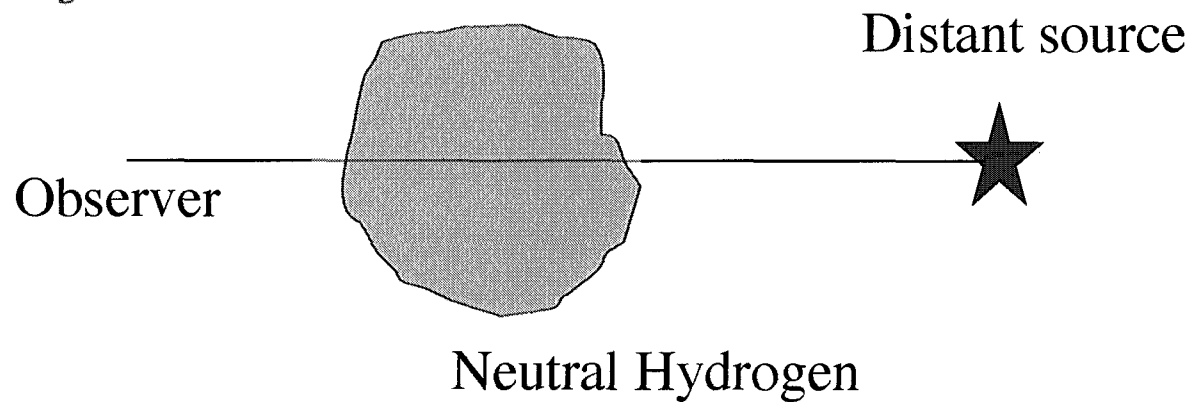


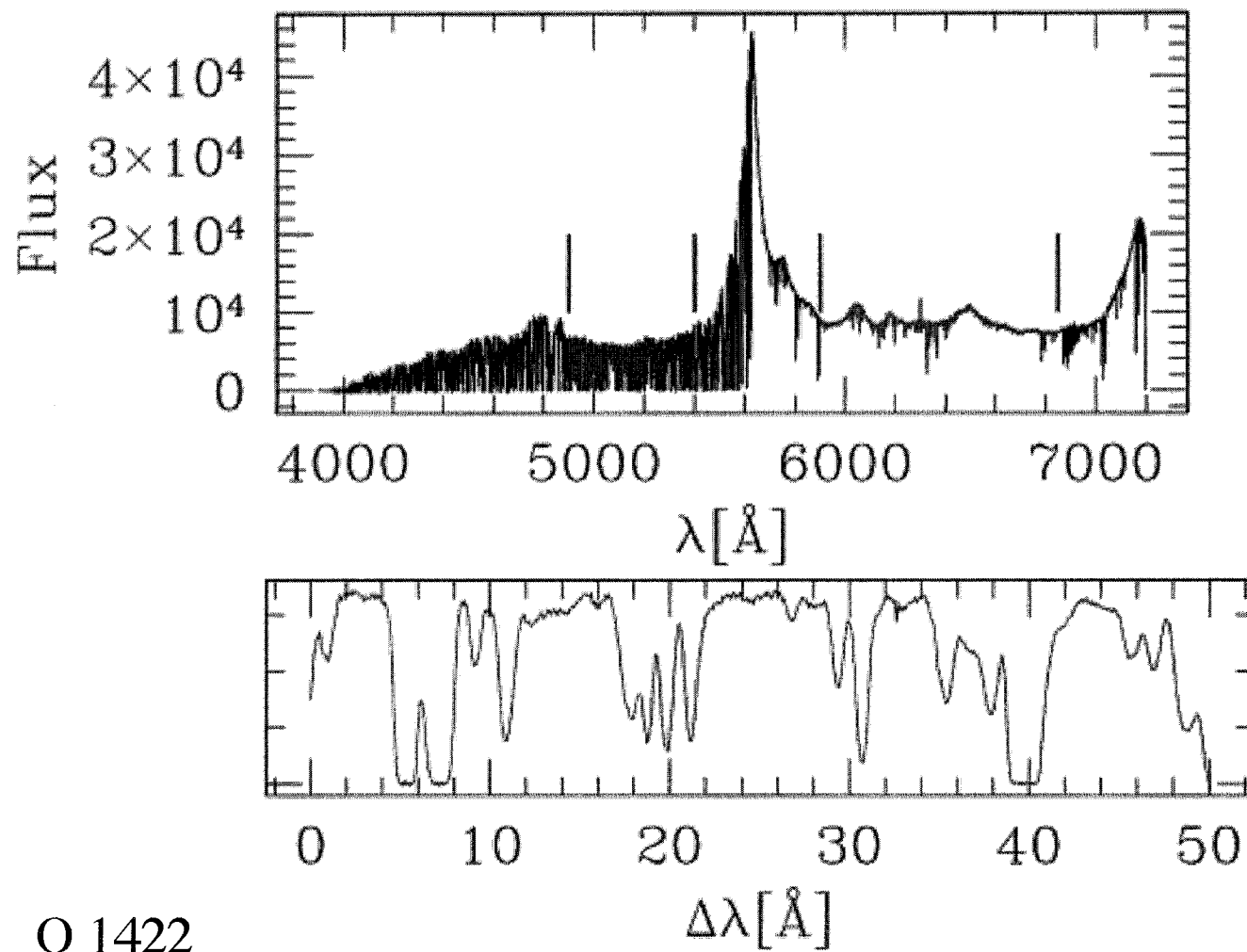
NCSA

The Lyman alpha optical depth

$$\tau_s = \frac{\pi e^2 f_\alpha \lambda_\alpha n_{\text{HI}}(z_s)}{m_e c H(z_s)} \approx 6.45 \times 10^5 x_{\text{HI}} \left(\frac{\Omega_b h}{0.03} \right) \left(\frac{\Omega_m}{0.3} \right)^{-1/2} \left(\frac{1+z_s}{10} \right)^{3/2}$$

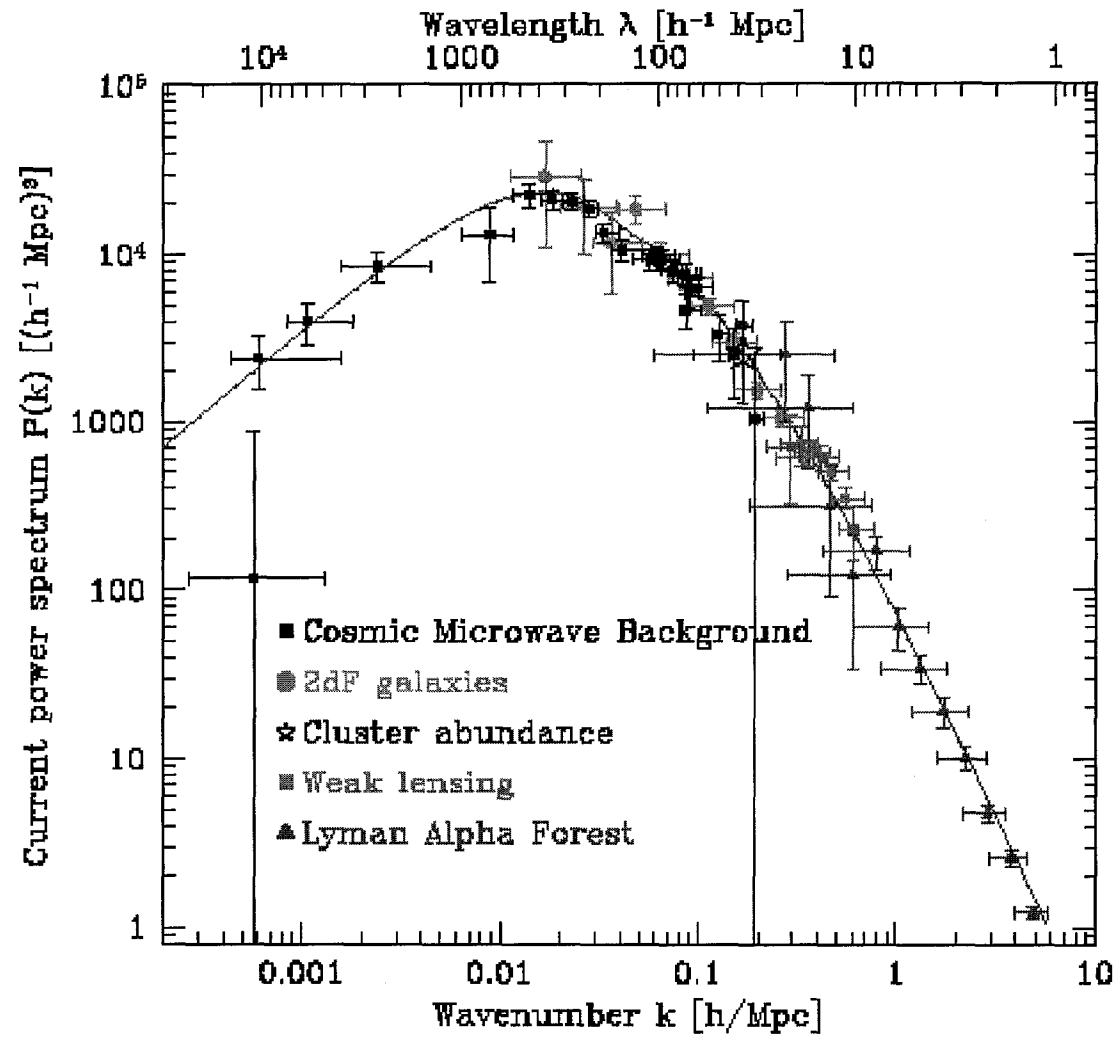
$$T = e^{-\tau_s}$$



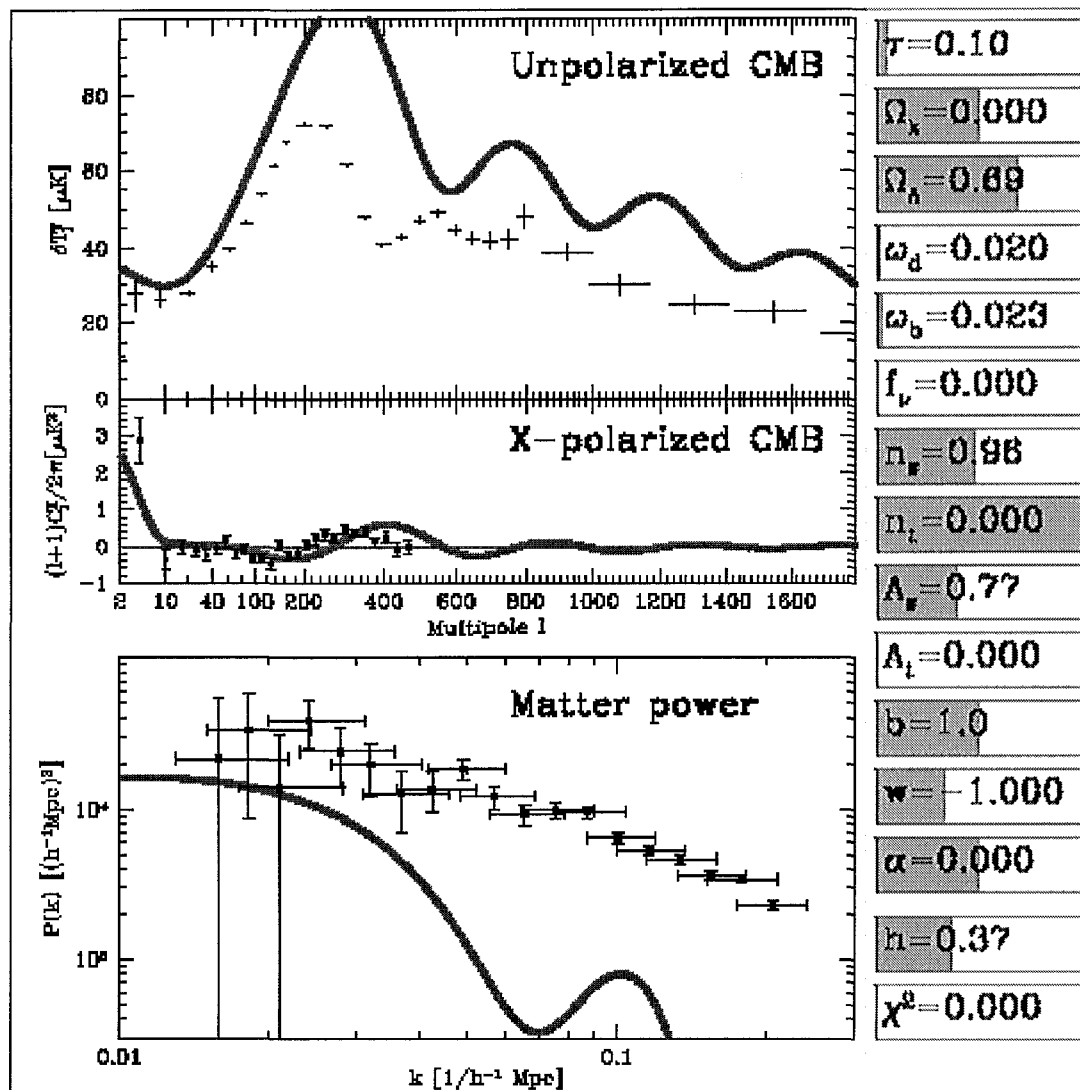


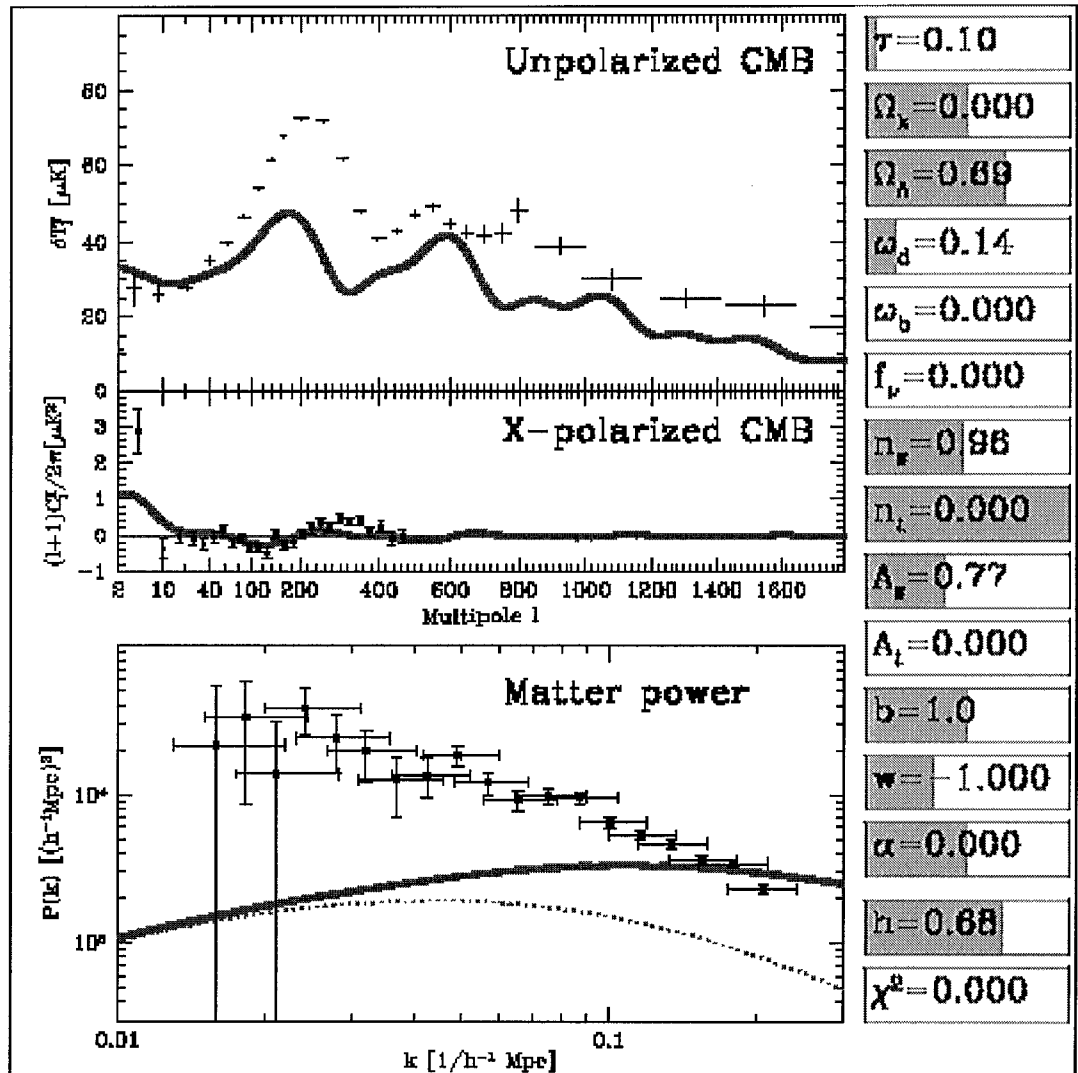
Q 1422
Songaila & Cowie

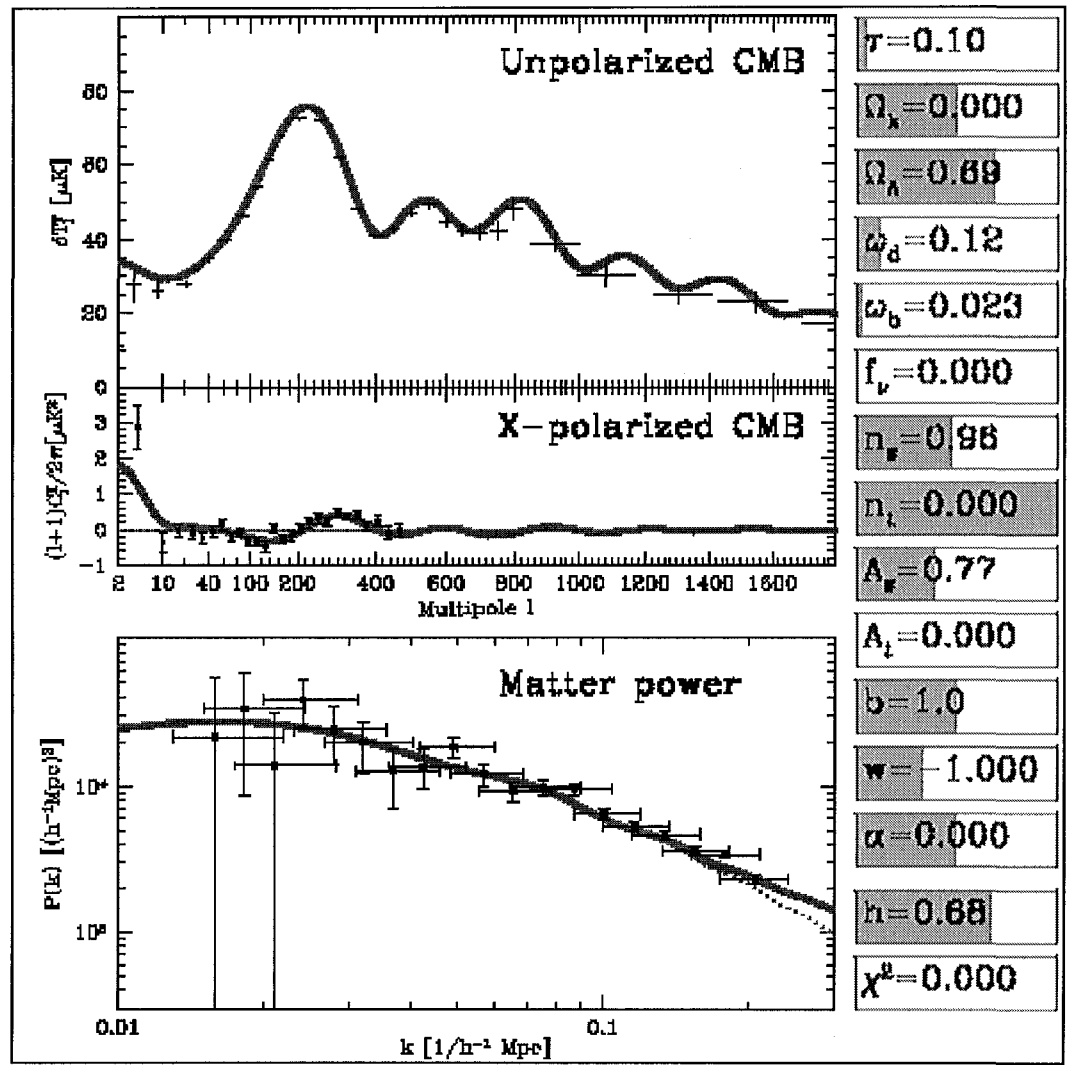
Inferred matter fluctuations at present epoch

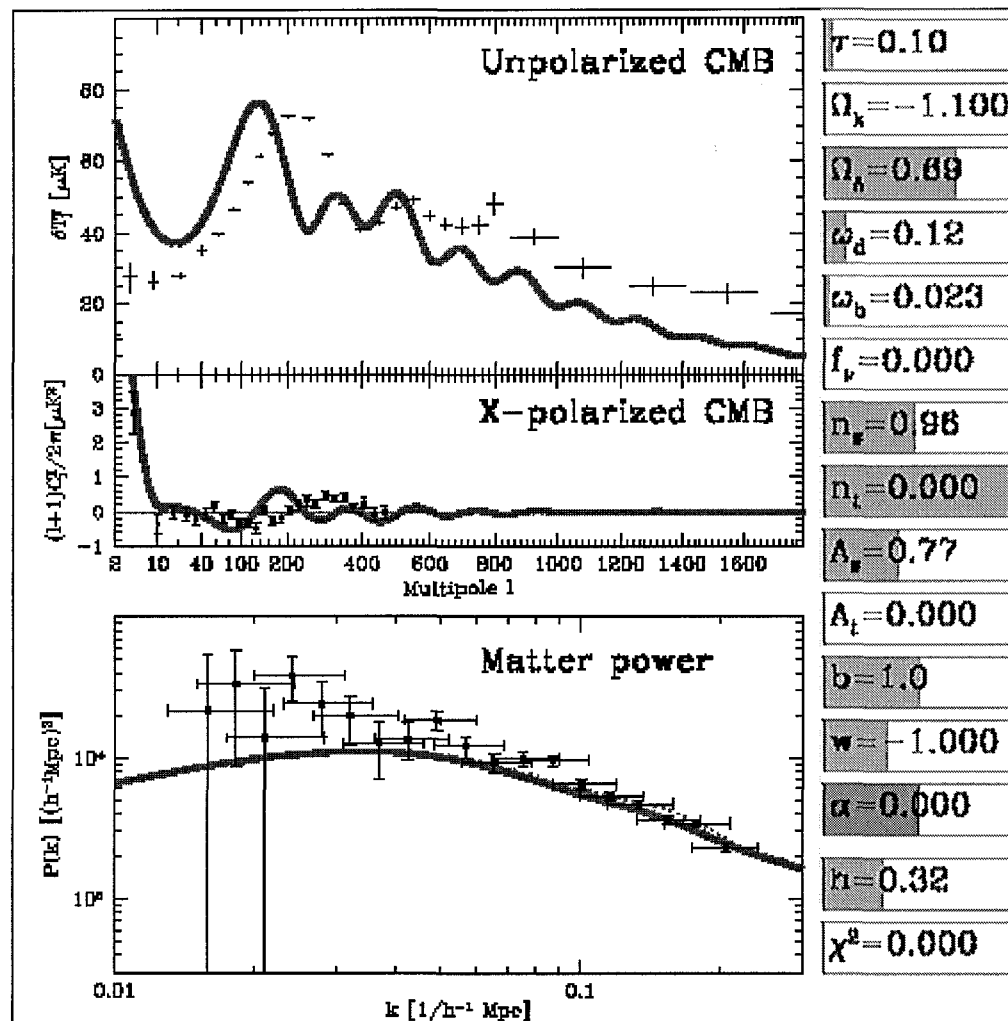


Tegmark & MZ









Tegmark et al.
 Constraints
 combining WMAP
 and SDSS

astro-ph/0310723

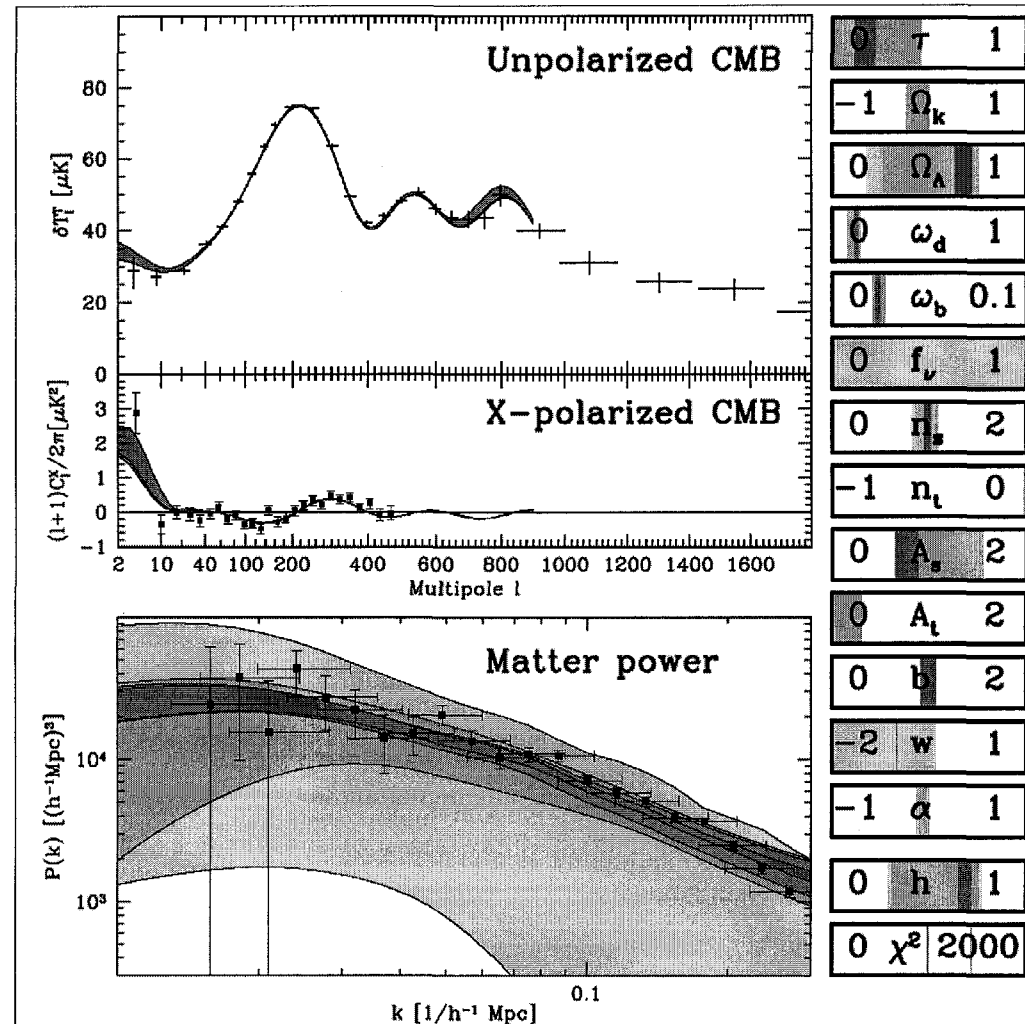


FIG. 1: Summary of observations and cosmological models. Data points are for unpolarized CMB experiments combined (top; Appendix A.3 details data used) cross-polarized CMB from WMAP (middle) and Galaxy power from SDSS (bottom). Shaded bands show the 1-sigma range of theoretical models from the Monte-Carlo Markov chains, both for cosmological parameters (right) and for the corresponding power spectra (left). From outside in, these bands correspond to WMAP with no priors, adding the prior $f_\nu = 0$, $w = -1$, further adding the priors $\Omega_k = \nu = \alpha = 0$, and further adding the SDSS information, respectively. These four bands essentially coincide in the top two panels, since the CMB constraints were included in the fits. Note that the l -axis in the upper two panels goes from logarithmic on the left to linear on the right, to show important features at both ends, whereas the k -axis of the bottom panel is simply logarithmic.

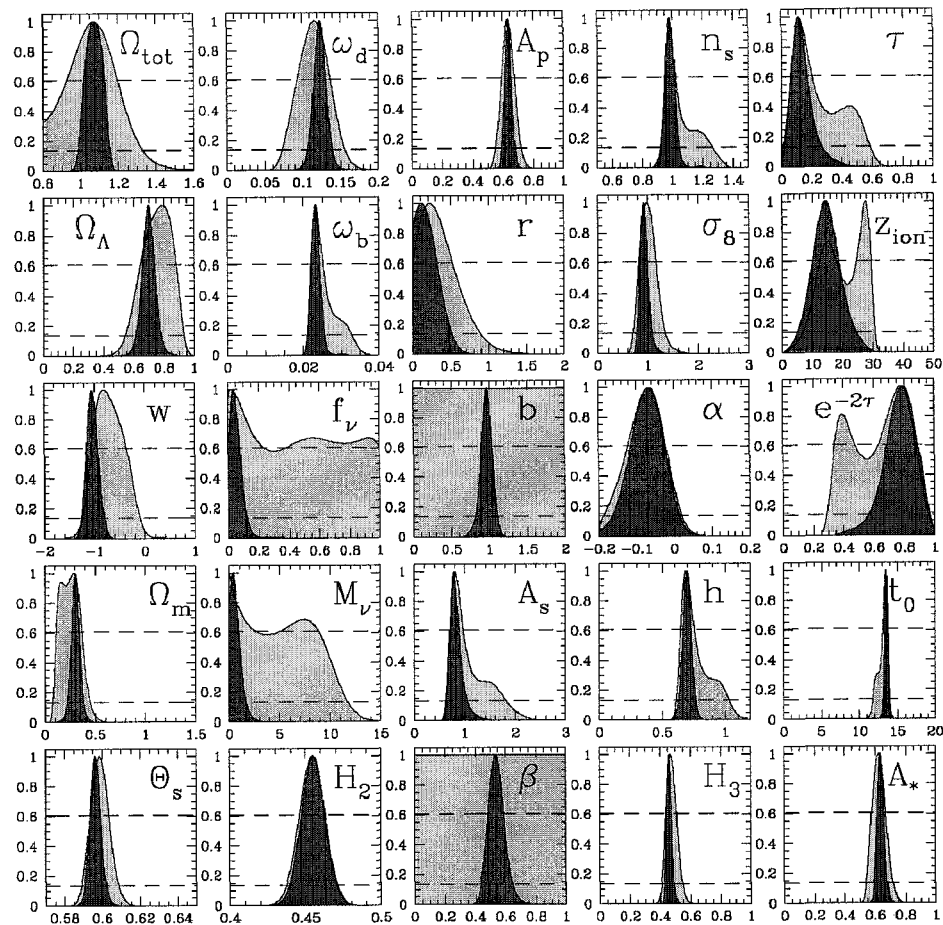


FIG. 2: Constraints on individual cosmological quantities using WMAP alone (shaded yellow/light grey distributions) and including SDSS information (narrower red/dark grey distributions). Each distribution shown has been marginalized over all other quantities in the class of 6-parameter $(\tau, \Omega_\Lambda, \omega_d, \omega_b, A_s, n_s)$ “vanilla” models as well as over a galaxy bias parameter b for the SDSS case. The α -distributions are also marginalized over r and Ω_b . The parameter measurements and error bars quoted in the tables correspond to the median and the central 68% of the distributions, indicated by three vertical lines for the WMAP+SDSS case above. When the distribution peaks near zero (like for r), we instead quote an upper limit at the 95th percentile (single vertical line). The horizontal dashed lines indicate $e^{-x^2/2}$ for $x = 1$ and 2 , respectively, so if the distribution were Gaussian, its intersections with these lines would correspond to 1σ and 2σ limits, respectively.

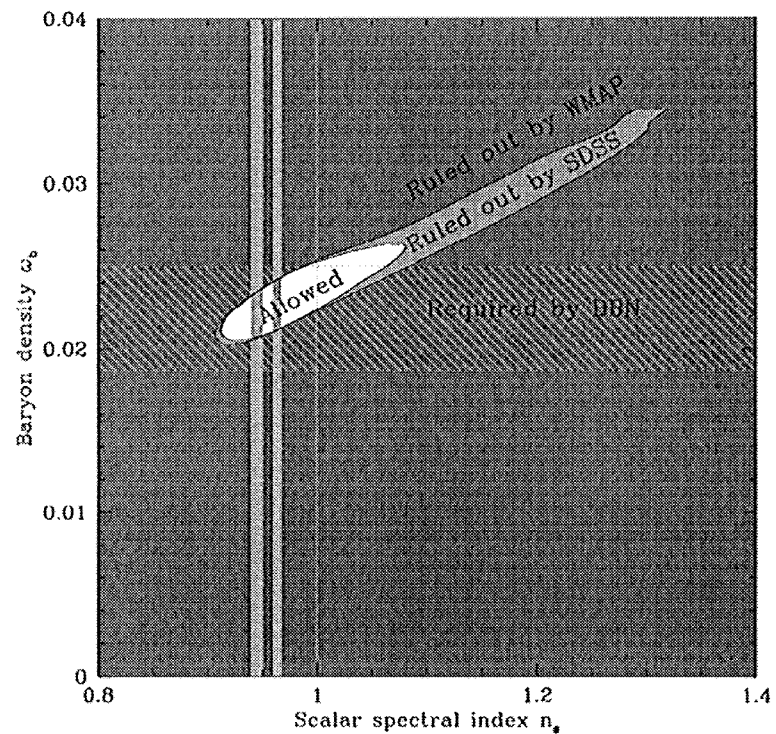


FIG. 3: 95% constraints in the (n_s, ω_b) plane. The shaded dark red/grey region is ruled out by WMAP alone for 6-parameter “vanilla” models, leaving the long degeneracy banana discussed in the text. The shaded light red/grey region is ruled out when adding SDSS information. The hatched band is required by Big Bang Nucleosynthesis (BBN). From right to left, the three vertical bands correspond to a scale-invariant Harrison-Zel’dovich spectrum and to the common inflationary predictions $n_s = 1 - 2/N \sim 0.96$ and $n_s = 1 - 3/N \sim 0.94$ (Table 6), assuming that the number of e-foldings between horizon exit of the observed fluctuations and the end of inflation is $50 < N < 60$.

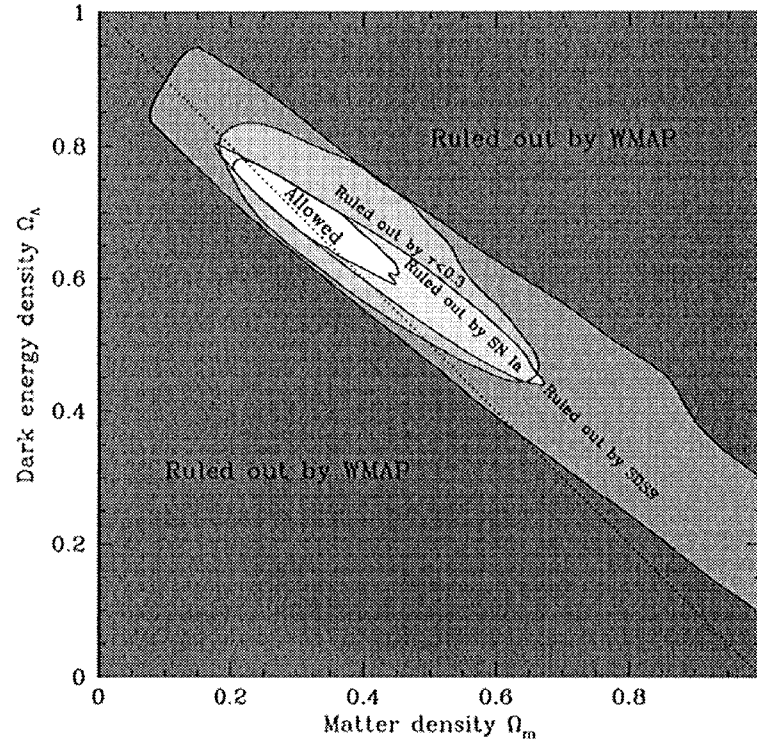


FIG. 9: 95% constraints in the $(\Omega_m, \Omega_\Lambda)$ plane. Shaded dark red/grey region is ruled out by WMAP alone for 7-parameter curved models, illustrating the well-known geometric degeneracy between models that all have the same acoustic peak locations. The shaded light red/grey region is ruled out when adding SDSS information. Continuing inwards, the next two regions are ruled out when adding the $\tau < 0.3$ assumption and when including SN Ia information as well. Models on the diagonal dotted line are flat, those below are open and those above are closed. The constraints in this plot agrees well with those in Figure 13 from [6] when taking the τ prior into account.

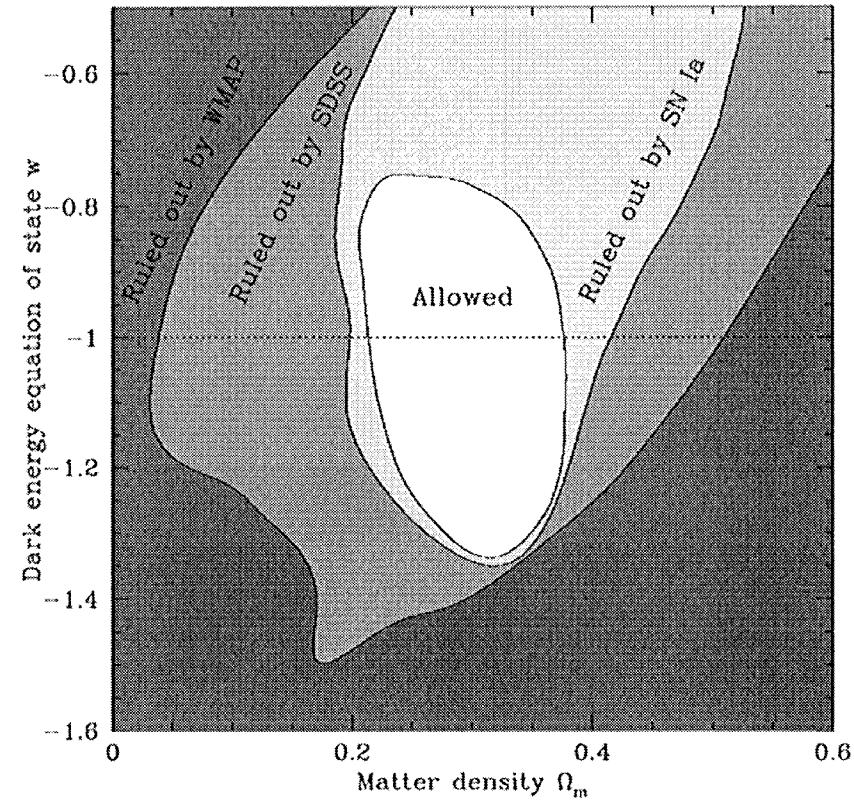


FIG. 13: 95% constraints in the (Ω_m, w) plane. Shaded dark red/grey region is ruled out by WMAP alone when equation of state w is added to the 6 “vanilla” parameters. The shaded light red/grey region is ruled out when adding SDSS information, and the yellow/very light grey region is excluded when including SN Ia information as well.

What to expect in the near future

Parameter constraints
from Lyman alpha
forest constraints of
SDSS quasars.

McDonald et al. (SDSS) astro-ph/0405013

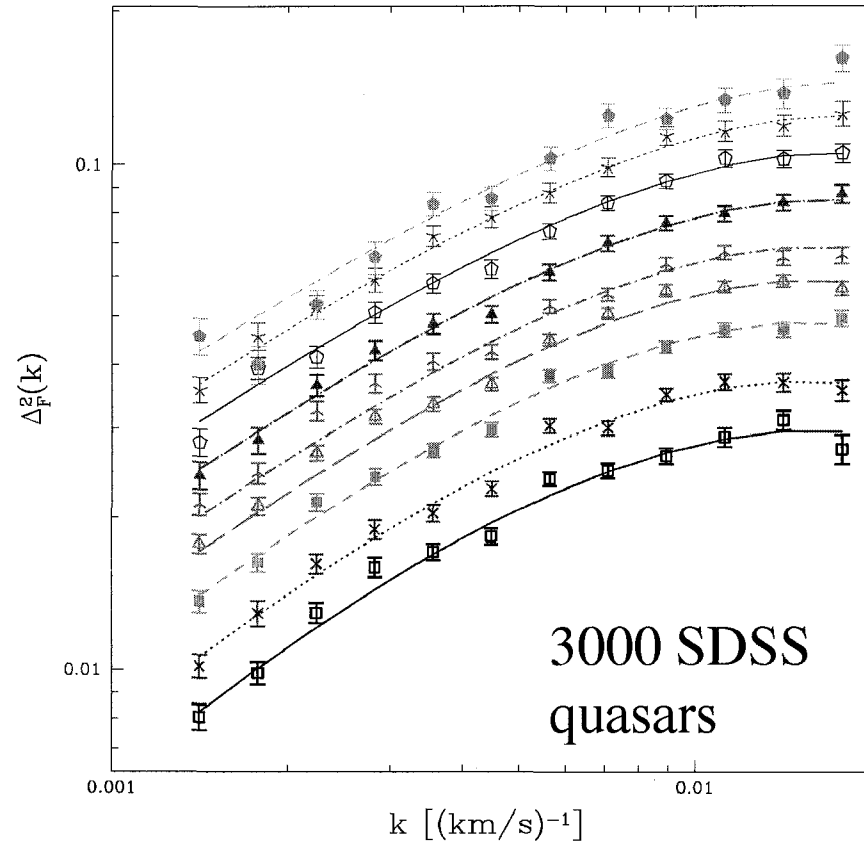


Fig. 21.— Points with error bars show the observed $P_P(k, z)$. Lines show our first attempt to fit a theoretical model, which is not a good fit to the data. From bottom to top — $z=2.2$: black, solid line, open square; $z=2.4$: blue, dotted line, 4-point star (cross); $z=2.6$: cyan, dashed line, filled square; $z=2.8$: green, long-dashed line, open triangle; $z=3.0$: magenta, dot-dashed line, 3-point star; $z=3.2$: red, dot-long-dashed line, filled triangle; $z=3.4$: black, thin solid line, open pentagon; $z=3.6$: blue, thin dotted line, 5-point star; $z=3.8$: cyan, thin dashed line, filled pentagon.

Secondary Anisotropies

Secondary anisotropies are those produced by the scattering of CMB photons along the line of sight after recombination

Secondary Anisotropies

They can be divided into two classes:

1. Actual scatterings with electrons:

- Thermal SZ Effect
- Kinetic SZ Effect
- Large angle polarization
- Patchy reionization

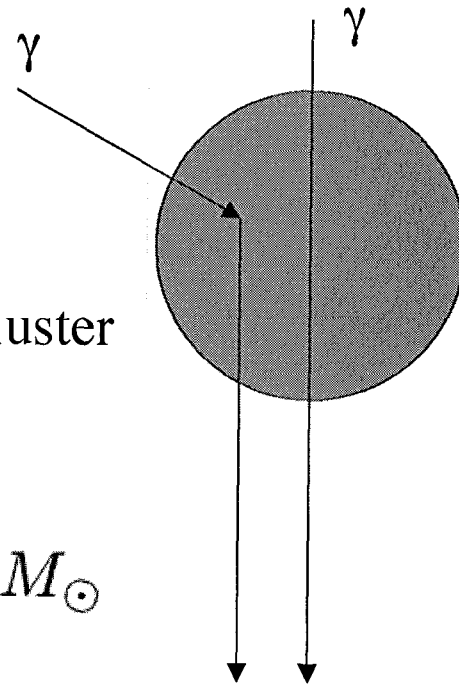
2. Gravitational secondaries:

- Time dependence of the potential: ISW effect, Rees Sciama effect, etc
- Gravitational Lensing

Thermal SZ effect

Hot gas in a cluster
of galaxies

$$M \sim 10^{14} M_{\odot}$$



Observer

$$L \sim 1 \text{ Mpc} \quad n_e \sim 3 \cdot 10^{-3} \text{ cm}^{-3}$$

$$n_e \sigma_T L \sim 10^{-2}$$

$$T \sim 10 \text{ keV}$$

$$\frac{\Delta E}{E} \sim \frac{kT}{m_e c^2} \sim 10^{-2}$$

$$y = \int dl n_e \sigma_T \left(\frac{kT}{m_e c^2} \right)$$

$$y \sim 10^{-4}$$

SZ spectral distortions

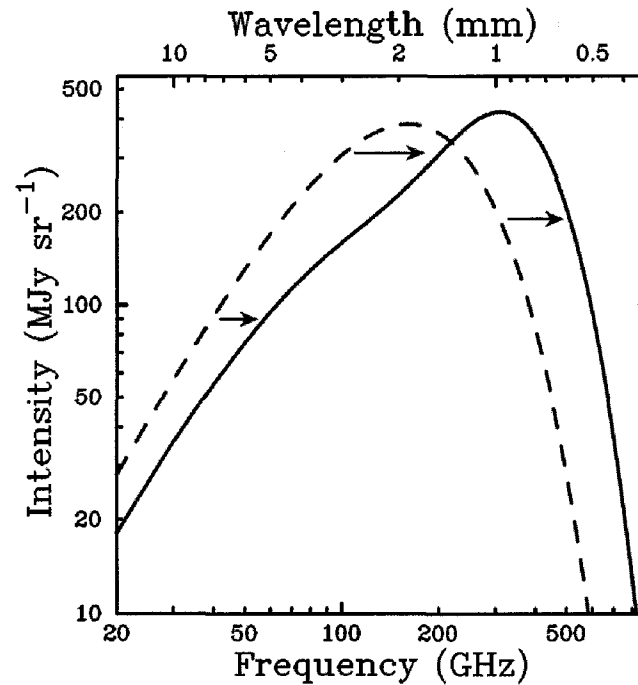


Figure 1: The Cosmic Microwave Background (CMB) spectrum, undistorted (dashed line) and distorted by the Sunyaev-Zel'dovich effect (SZE) (solid line). Following Sunyaev & Zel'dovich (1980a) to illustrate the effect, the SZE distortion shown is for a fictional cluster 1000 times more massive than a typical massive galaxy cluster. The SZE causes a decrease in the CMB intensity at frequencies $\lesssim 218$ GHz and an increase at higher frequencies.

Carlstrom, Holder & Reese

SZ spectral distortions

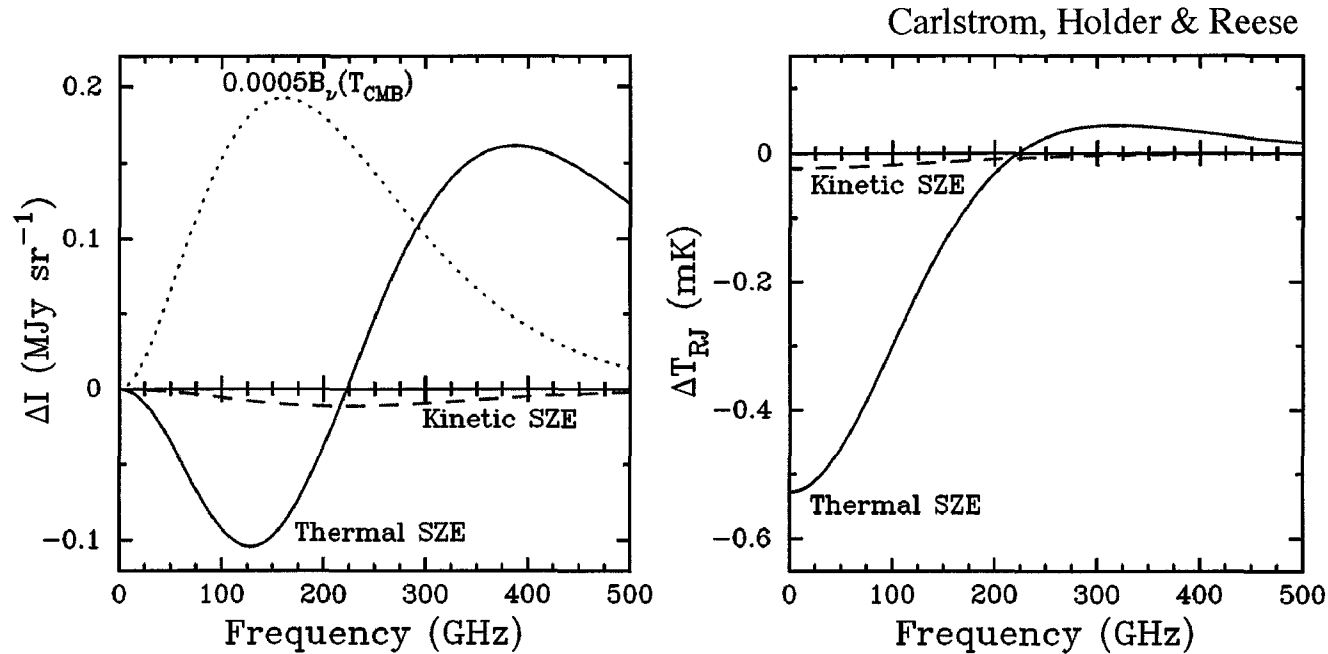
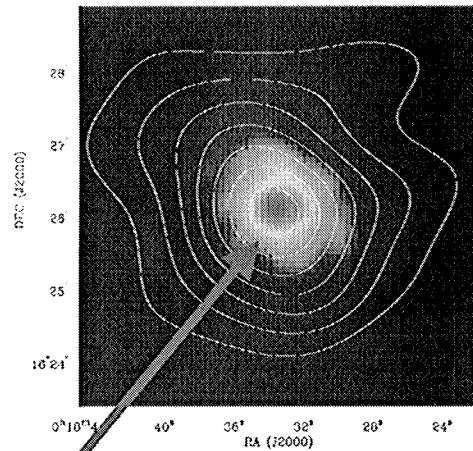
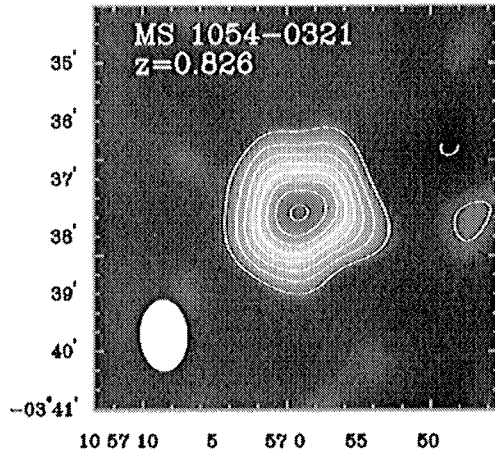


Figure 2: Spectral distortion of the cosmic microwave background (CMB) radiation due to the Sunyaev-Zel'dovich effect (SZE). The left panel shows the intensity and the right panel shows the Rayleigh Jeans brightness temperature. The thick solid line is the thermal SZE and the dashed line is the kinetic SZE. For reference the 2.7 K thermal spectrum for the CMB intensity scaled by 0.0005 is shown by the dotted line in the left panel. The cluster properties used to calculate the spectra are an electron temperature of 10 keV, a Compton y parameter of 10^{-4} , and a peculiar velocity of 500 km s^{-1} .

SZ Images



X-ray

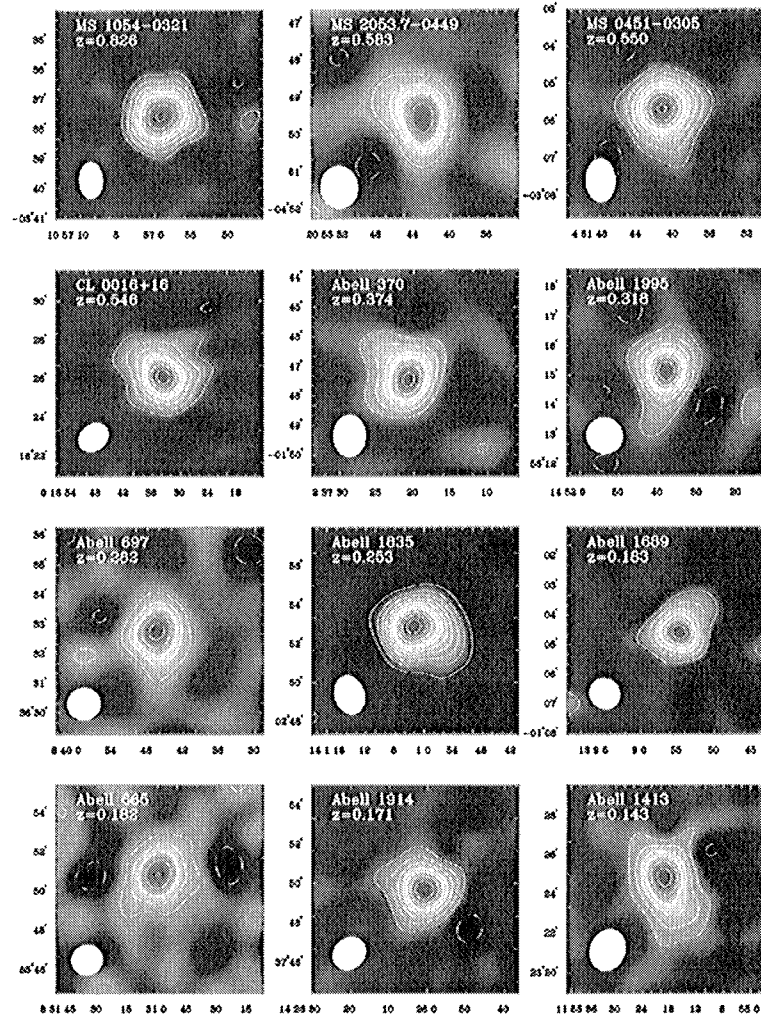
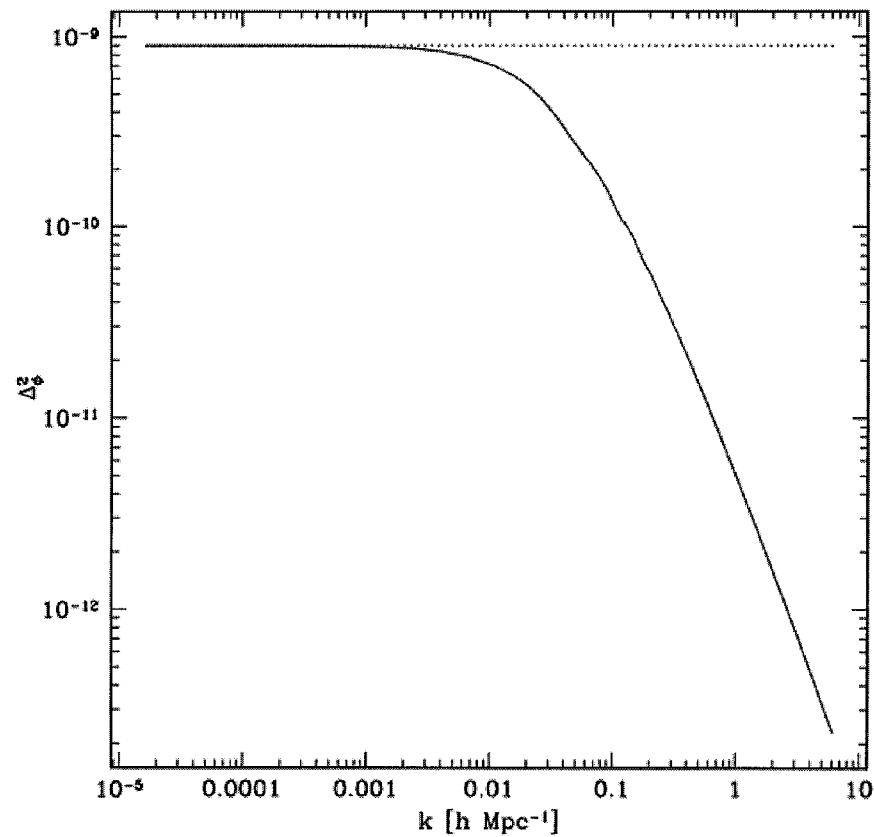


Figure 3: Images of the Sunyaev-Zel'dovich effect toward twelve distant clusters with redshifts spanning 0.83 (top left) to 0.14 (bottom right). The evenly spaced contours are multiples starting at ± 1 of 1.5σ to 3σ depending on the cluster, where σ is the rms noise level in the images. The noise levels range from 15 to 40 μK . The data were taken with the OVRO and BIMA mm-arrays outfitted with low-noise cm-wave receivers. The filled ellipse shown in the bottom left corner of each panel represents the FWHM of the effective resolution used to make these images.

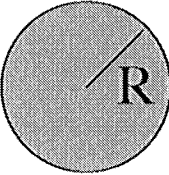
The power spectrum of the potential: decay during the radiation era



Structure formation

$$\nabla^2 \phi = 4\pi G a^2 \bar{\rho} \delta$$

$$k^2 \phi = \frac{3}{2} H^2 \Omega_m a^2 \delta$$

$$M = \frac{4\pi G}{3} \bar{\rho} R^3$$


$$\delta \propto a ; \quad \phi \propto \text{const.}$$

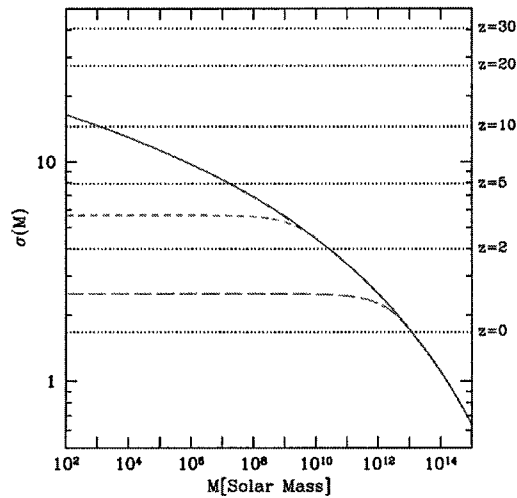
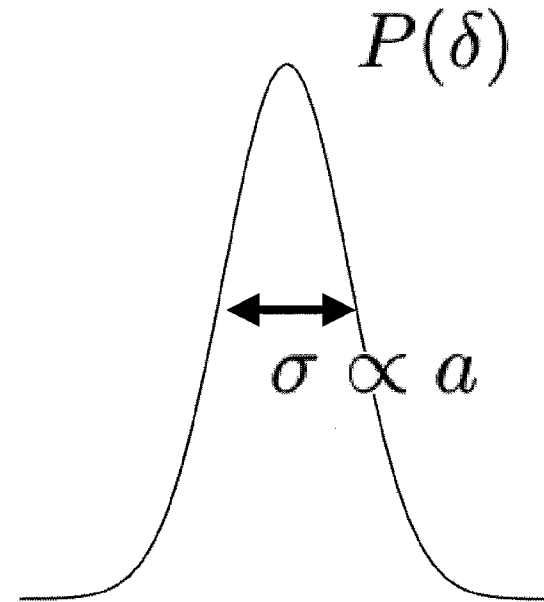


Fig. 5.— Mass fluctuations and collapse thresholds in cold dark matter models. The horizontal dotted lines show the value of the extrapolated collapse overdensity $\delta_{\text{crit}}(z)$ at the indicated redshifts. Also shown is the value of $\sigma(M)$ for the cosmological parameters given in the text (solid curve), as well as $\sigma(M)$ for a power spectrum with a cutoff below a mass $M = 1.7 \times 10^6 M_{\odot}$ (short-dashed curve), or $M = 1.7 \times 10^{11} M_{\odot}$ (long-dashed curve). The intersection of the horizontal lines with the other curves indicate, at each redshift z , the mass scale (for each model) at which a $1 - \sigma$ fluctuation is just collapsing at z (see the discussion in the text).



Structure formation

When do objects form?

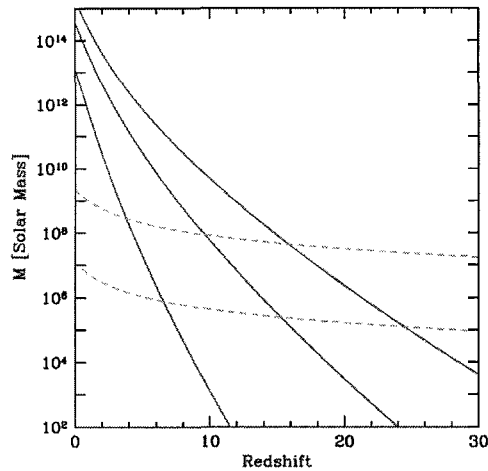


Fig. 6.— Characteristic properties of collapsing halos: Halo mass. The solid curves show the mass of collapsing halos which correspond to $1-\sigma$, $2-\sigma$, and $3-\sigma$ fluctuations (in order from bottom to top). The dashed curves show the mass corresponding to the minimum temperature required for efficient cooling with primordial atomic species only (upper curve) or with the addition of molecular hydrogen (lower curve).

Barkana & Loeb

What is the distribution of masses ?

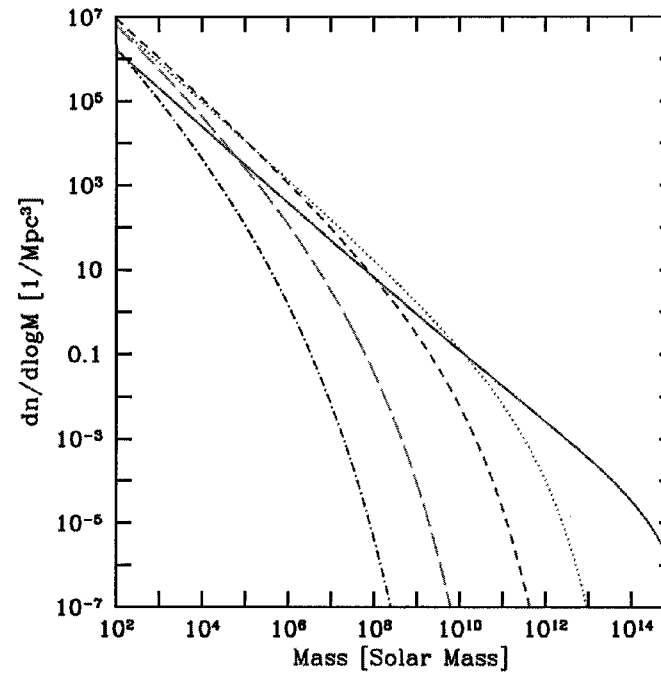


Fig. 10.— Halo mass function at several redshifts: $z = 0$ (solid curve), $z = 5$ (dotted curve), $z = 10$ (short-dashed curve), $z = 20$ (long-dashed curve), and $z = 30$ (dot-dashed curve).

Cosmology with SZ

Clusters

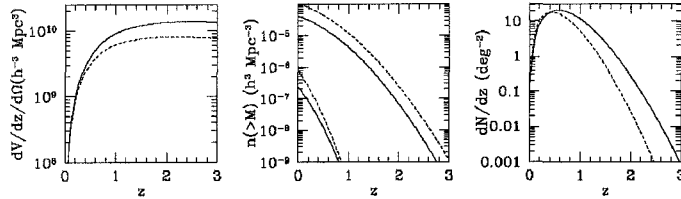


Figure 7: Comoving volume element (left) and comoving number density (center) for two cosmologies, $(\Omega_M, \Omega_\Lambda) = (0.3, 0.7)$ (solid) and $(0.5, 0.5)$ (dashed). For the middle panel, the normalization of the matter power spectrum was taken to be $\sigma_8 = 0.9$ and the Press-Schechter mass function was assumed. The lower set of lines in the middle panel correspond to clusters with mass greater than $10^{15} h^{-1} M_\odot$ while the upper lines correspond to clusters with mass greater than $10^{14} h^{-1} M_\odot$. The right panel corresponds to the cluster redshift distribution per square degree for clusters with masses greater than $10^{14} h^{-1} M_\odot$, with the normalization of the power spectrum adjusted ($\sigma_8 = 0.75$ for $\Omega_M = 0.5$) to produce the same local cluster abundance for both cosmologies. Note that in this case, fewer clusters are predicted at high redshift for the higher density cosmology.

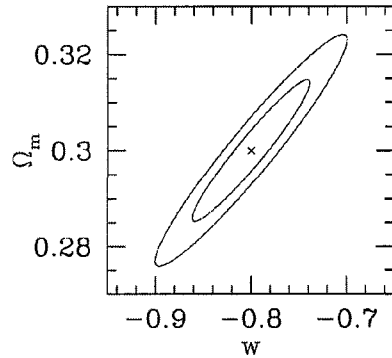


Figure 12: Expected constraints on the matter density Ω_M and the dark energy equation of state w from the analysis of a SZE survey covering several thousand square degrees in which all clusters above $2.5 \times 10^{14} h^{-1} M_\odot$ are detected and the redshifts are known. The normalization of the power spectrum has been marginalized over, and contours show 68% and 95% confidence regions for two parameters. Note, that no systematic errors have been assumed in deriving the cosmological constraints. As discussed in the text, considerable observational and theoretical work needs to be done before such tight constraints could be extracted from large scale SZE surveys.

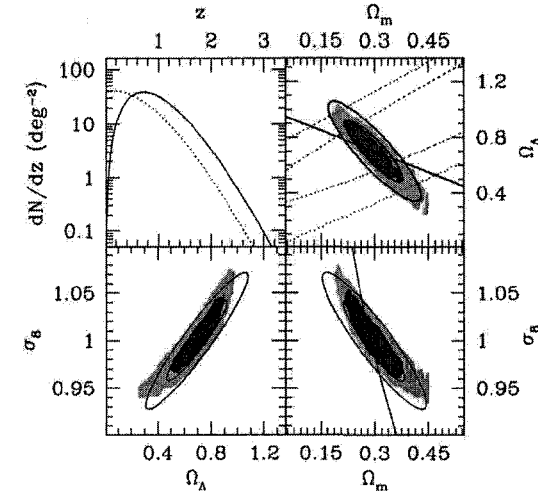
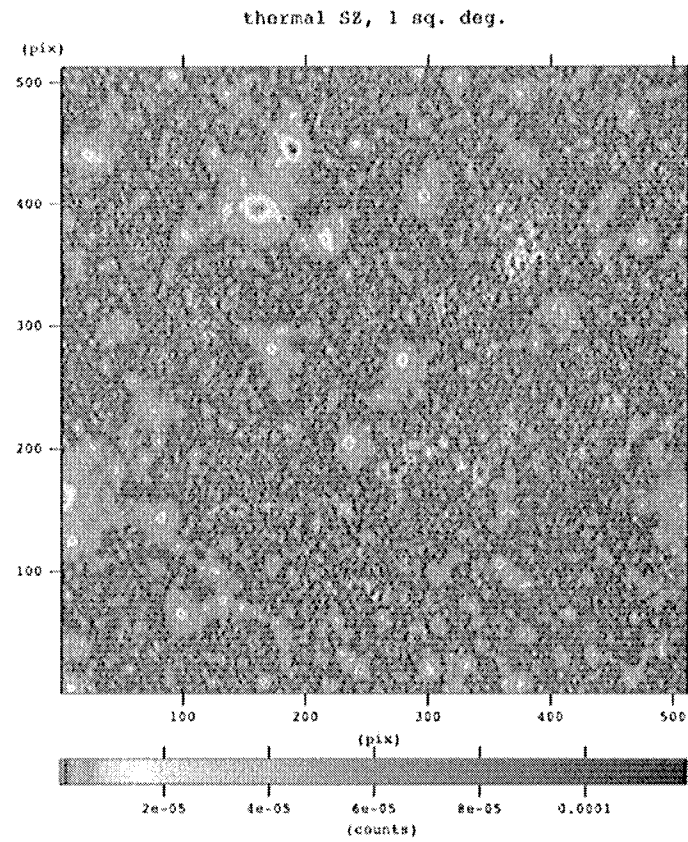


Figure 11: Expected constraints in the Ω_M - Ω_Λ (top right), Ω_M - σ_8 (bottom right), and Ω_Λ - σ_8 (bottom left) planes from the analysis of a SZE survey covering 12 square degrees in which all clusters above $10^{14} h^{-1} M_\odot$ are detected and the redshifts are known. The top left panel shows the expected redshift distribution of clusters (solid line) with the cumulative $N(> z)$ shown as a dotted line. In the other panels, the 68% confidence regions are shown by the darkest shaded regions, and the 95% confidence by the lighter regions. The solid contours correspond to the same confidence regions derived from an approximate method. In each panel the dimension not shown has been marginalized over rather than kept fixed. In the upper right panel, the broken line diagonal ellipses are the constraints based on the analyses of type Ia Supernova at 68% and 95% confidence (Riess et al 1998; Perlmutter et al 1999). The diagonal line at $\Omega_M + \Omega_\Lambda = 1$ is for a flat universe as suggested by recent CMB anisotropy measurements (Miller et al 1999; de Bernardis et al 2000; Hanany et al 2000; Pryke et al 2002). The solid line in lower right panel shows the approximate direction of current constraints (Viana & Liddle 1999).

SZ by LSS



Observational Status

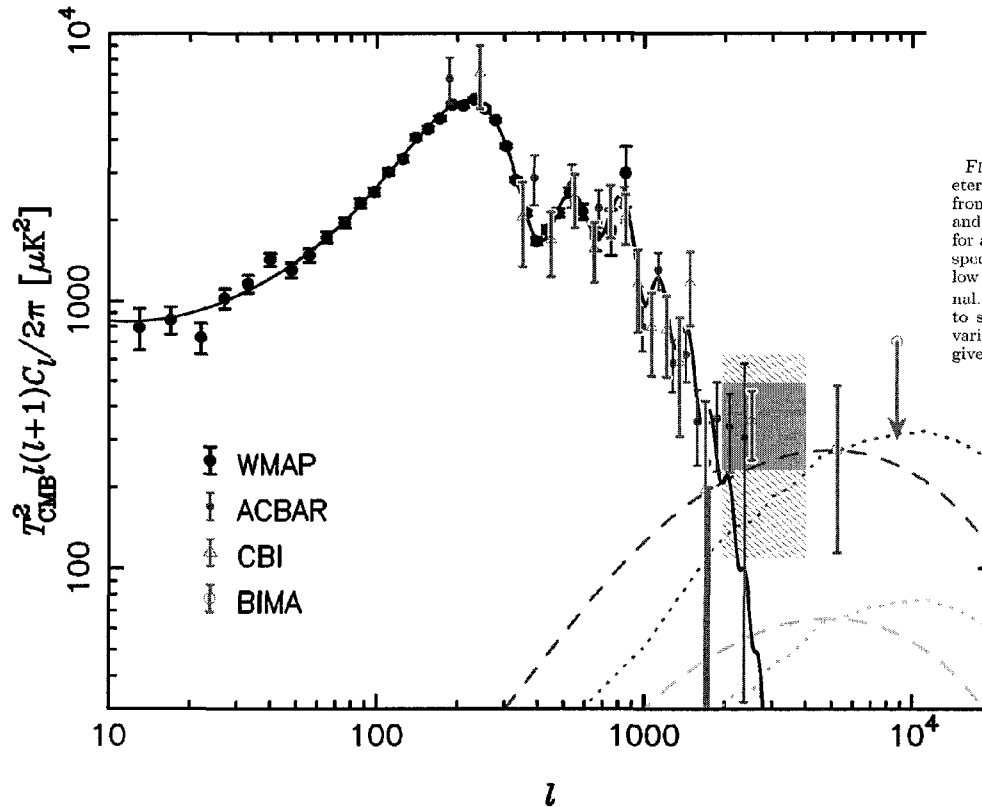


FIG. 14.— The CBI+*WMAP*+ACBAR Spectrum + high ℓ points from BIMA. The curves at high ℓ show the levels of SZ power expected in representative models using moving mesh hydrodynamics simulations (dotted) and smooth particle hydrodynamics (dashed) simulations (see text). The green and pink curves correspond to 30 GHz and 150 GHz, respectively. In these simulations $\sigma_8^{SZ} = 0.98$, which also fits well the *WMAP* and CBI observations at lower ℓ for the case of a running spectral index (see Table 5). The highest- ℓ ACBAR point has been displaced slightly to lower ℓ for clarity.

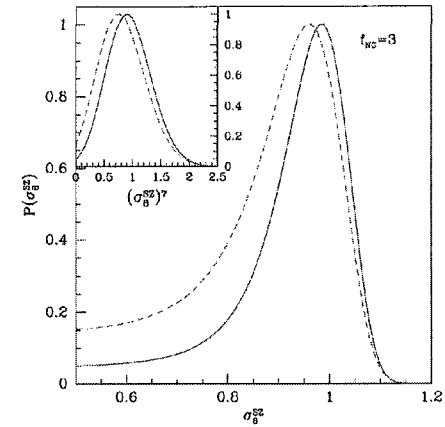


FIG. 12.— Constraints on secondary SZE anisotropy, as parameterized by the effective parameter σ_8^{SZ} . The curves are obtained from fits to the data at $\ell > 2000$ (CBI and BIMA (red dashed), and CBI, BIMA, and ACBAR (blue solid)). The fitting accounts for a separate contributions from template primary and secondary spectra. The marginalized distribution is heavily skewed towards low σ_8^{SZ} values due to the assumed scaling of the secondary signal. In the inset we have plotted the distribution against $(\sigma_8^{SZ})^7$ to show how the distribution is approximately Gaussian in this variable, which roughly corresponds to the high- ℓ bandpower in a given experiment.

Scattering secondaries

$$\frac{\delta T}{T}(\hat{\mathbf{n}}) = - \int dl n_e \sigma_T \hat{\mathbf{n}} \cdot \mathbf{v}$$

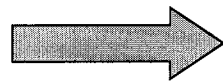
$$n_e = x_e (1 + \delta) \bar{n}_b$$

Ionized fraction

overdensity

mean density

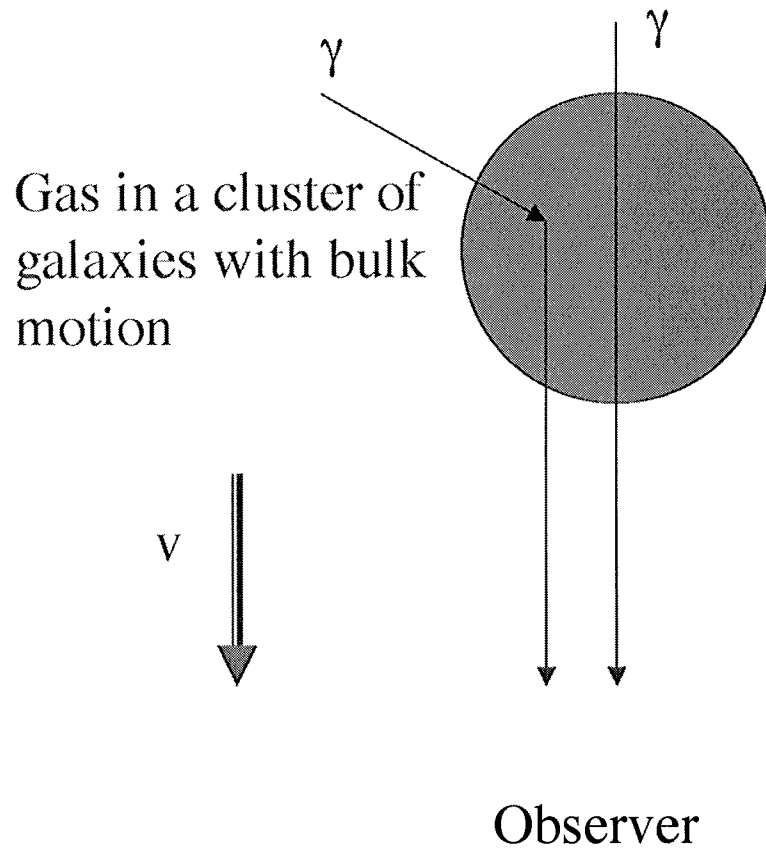
$$\mathbf{v} = \nabla \psi$$



Cancellations along the line of sight

Kinetic SZ effect

$$L \sim 1 \text{ Mpc} \quad n_e \sim 3 \cdot 10^{-3} \text{ cm}^{-3}$$



$$n_e \sigma_T L \sim 10^{-2}$$

$$\frac{\Delta \nu}{\nu} = \frac{v}{c} \sim 3 \cdot 10^{-3}$$

$$\frac{\Delta T}{T} = - \int dl n_e \sigma_T \frac{v}{c}$$

$$\frac{\Delta T}{T} = 10^{-5}$$

Patchy reionization

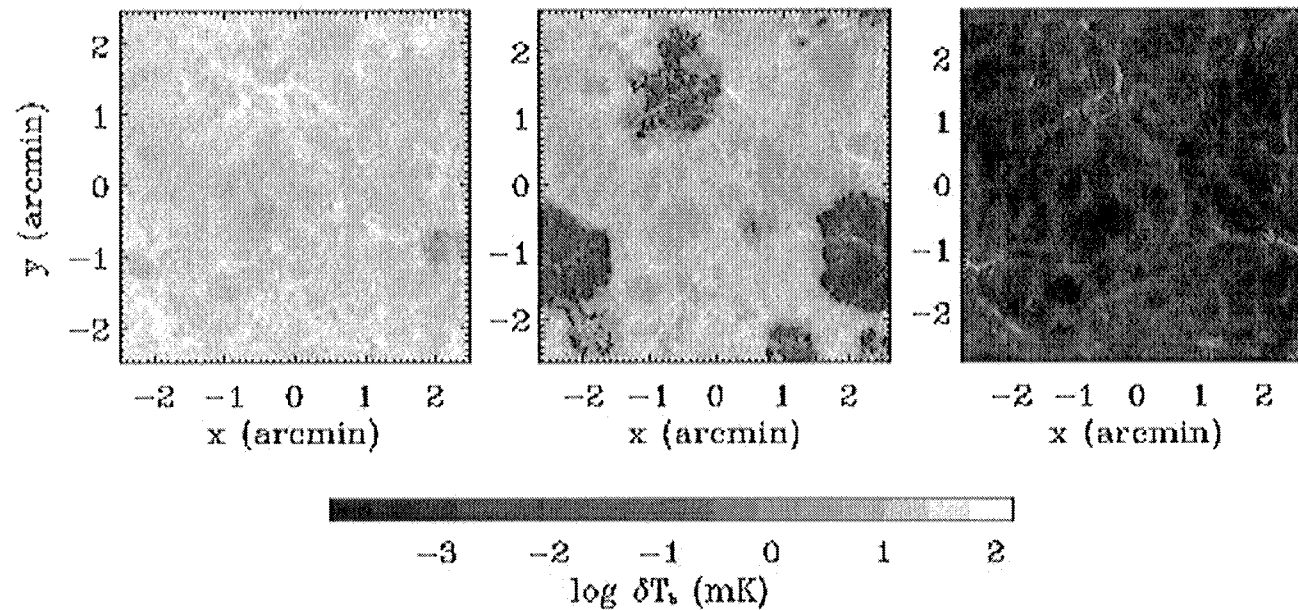
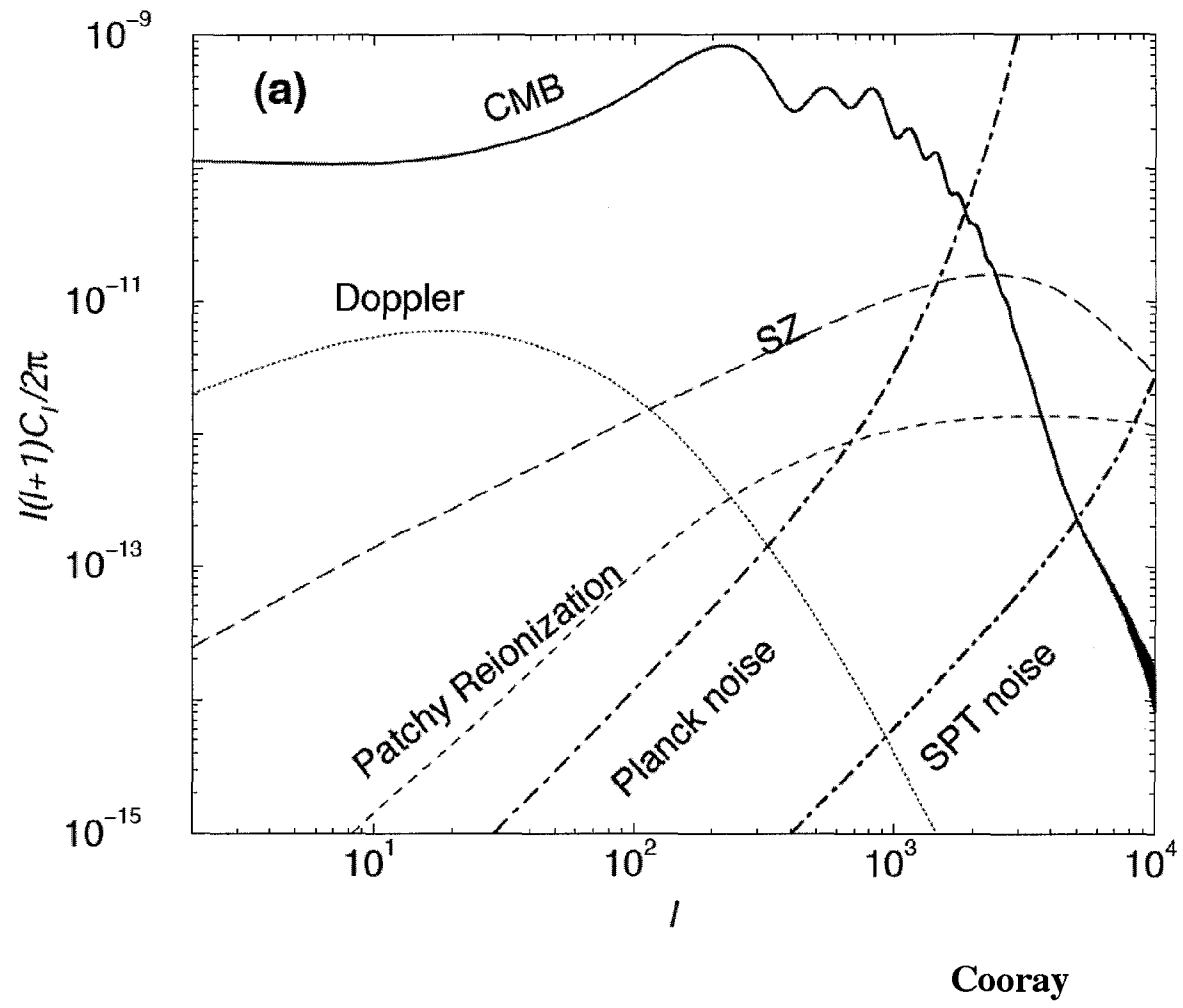


FIG. 1. — The brightness temperature of the 21 cm transition at several redshifts, as predicted by the “late reionization” simulation analyzed in Furlanetto et al. (2003). Each panel corresponds to the same slice of the simulation box (with width $10h^{-1}$ comoving Mpc and depth $\Delta\nu = 0.1$ MHz), at $z = 12.1$, 9.2, and 7.6, from left to right. The three epochs shown correspond to the early, middle, and late stages of reionization in this simulation. (For details about the simulations, see Sokasian et al. 2001; Springel & Hernquist 2003a,b.)

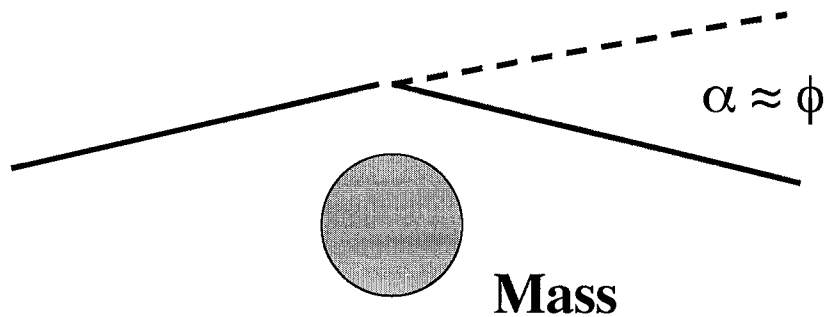


Gravitational secondaries

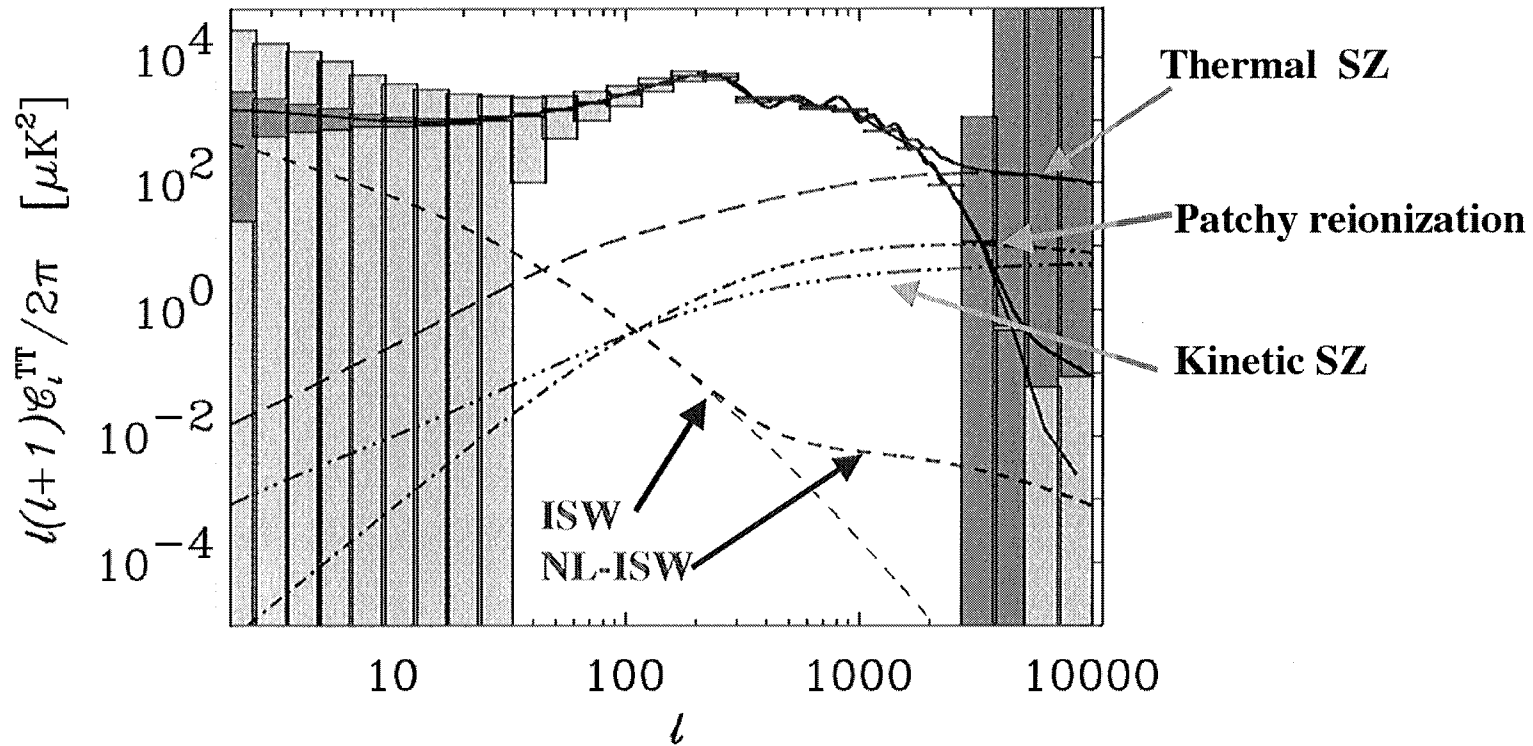
$$\frac{\delta T}{T} = \int dl (\dot{\phi} + \dot{\psi})$$

“ISW like effect”

“Gravitational lensing”

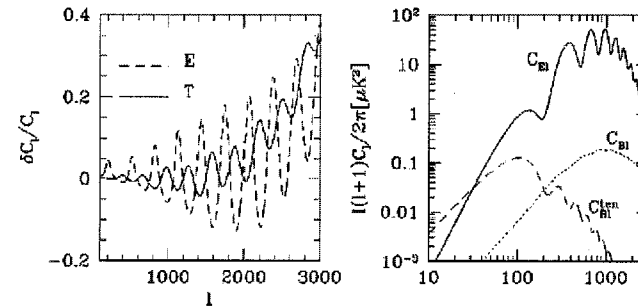
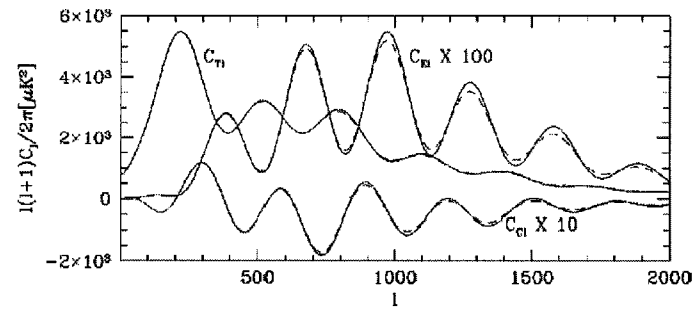
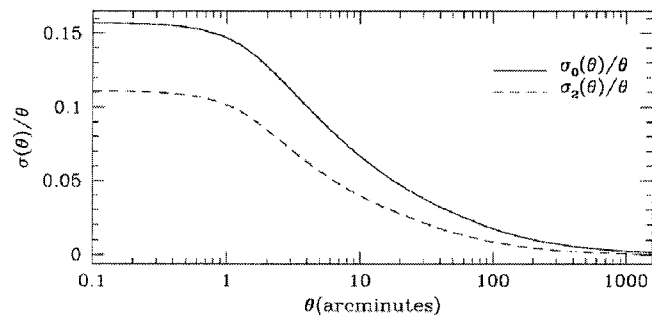
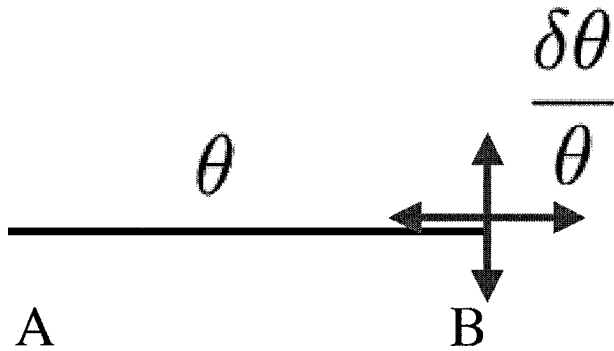


Secondary anisotropies: TT



Dore, Hennawi & Spergel

Gravitational lensing



Reconstructing the mass

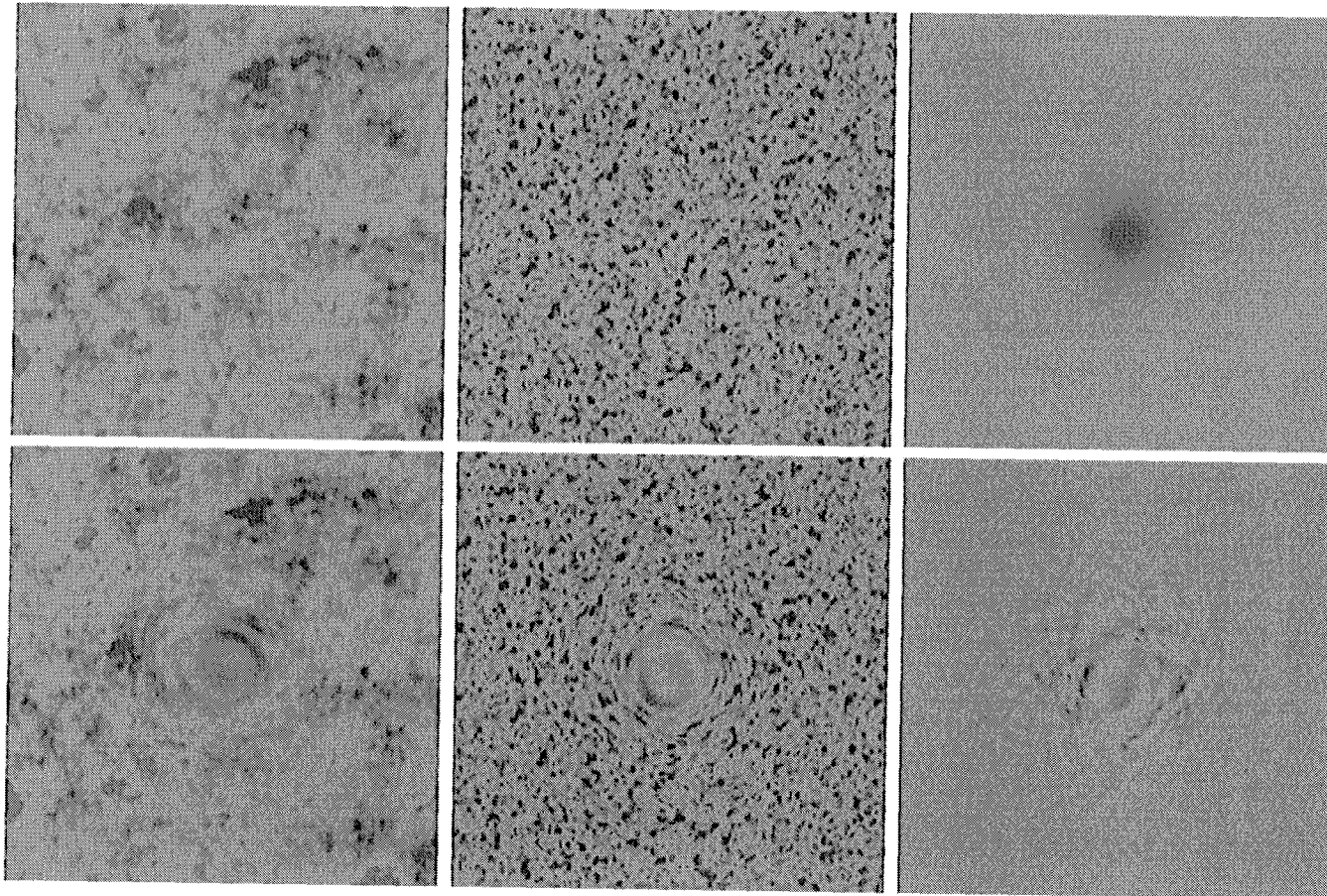


FIG. 1.— An exaggerated example of the lensing effect on a $10^\circ \times 10^\circ$ field. Top: (left-to-right) un lensed temperature field, un lensed E -polarization field, spherically symmetric deflection field $d(\mathbf{n})$. Bottom: (left-to-right) lensed temperature field, lensed E -polarization field, lensed B -polarization field. The scale for the polarization and temperature fields differ by a factor of 10.

W. Hu

TABLE V:

CMB	Cosmic Shear	w_0	w_a	m_ν	$ \ln \Omega_m h^2 $	$ \ln P_\Phi $	n_S	n'_S	τ	$ \ln \omega_b $	Y_P	θ_s
Planck	none	2.2	3.3	0.18	0.0084	0.017	0.0078	0.0035	0.010	0.0086	0.013	0.00016
	S300	0.16	0.26	0.074	0.0061	0.015	0.0065	0.0033	0.0090	0.0073	0.011	0.00014
	S1000	0.10	0.16	0.051	0.0048	0.015	0.0058	0.0031	0.0089	0.0067	0.011	0.00014
	G2 π	0.031	0.053	0.019	0.0033	0.014	0.0037	0.0020	0.0080	0.0058	0.0067	0.00012
	G4 π	0.022	0.040	0.014	0.0030	0.013	0.0033	0.0017	0.0074	0.0056	0.0059	0.00011
CMBpol	none	0.79	1.1	0.048	0.0040	0.017	0.0031	0.0018	0.0097	0.0028	0.0048	4.8×10^{-5}
	S300	0.12	0.20	0.044	0.0036	0.012	0.0029	0.0018	0.0073	0.0028	0.0046	4.6×10^{-5}
	S1000	0.082	0.13	0.037	0.0033	0.011	0.0028	0.0018	0.0066	0.0028	0.0046	4.5×10^{-5}
	G2 π	0.028	0.047	0.017	0.0022	0.0086	0.0024	0.0014	0.0053	0.0026	0.0037	3.9×10^{-5}
	G4 π	0.021	0.035	0.013	0.0021	0.0080	0.0021	0.0013	0.0049	0.0025	0.0033	3.6×10^{-5}

NOTES.—Forecasts of $1\text{-}\sigma$ errors for the combination of tomographic shear-shear two-point functions and the ratio statistic with Planck (upper table) and CMBpol (lower table)

$$\omega(a) = \omega_0 + \omega_a(1 - a)$$

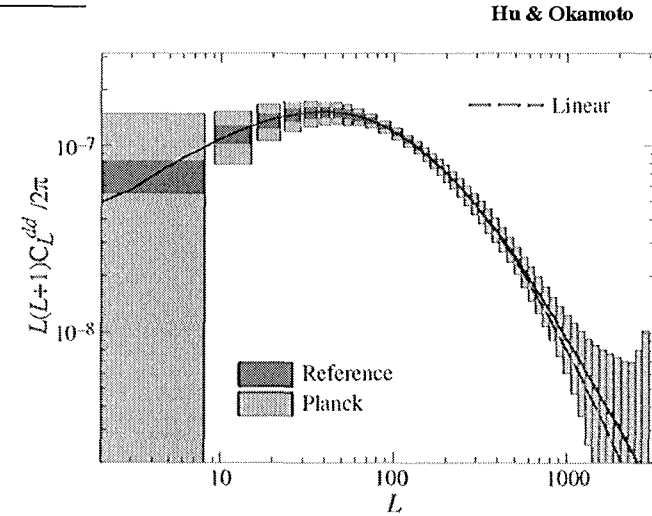


FIG. 6.— Statistical errors achievable on the deflection power spectrum with the Planck ($f_{\text{sky}} = 0.65$) and reference experiments ($f_{\text{sky}} = 1$). Boxes represent band averaging width and 1σ errors. The polarization information in the reference experiment allows for a cosmic variance limited measurement of the projected power spectrum out to $L \sim 1000$. In this regime, the fluctuations are almost completely linear (dashed lines).

THE END

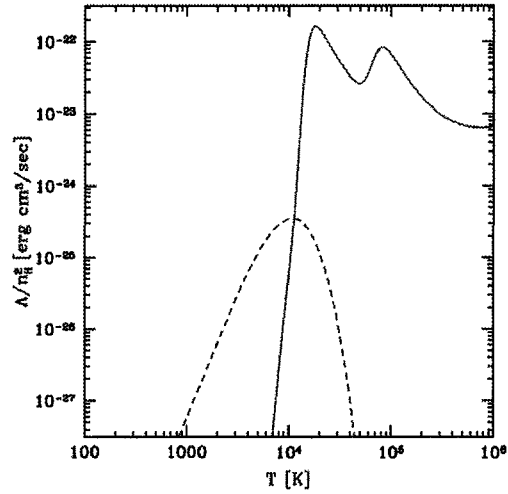


Fig. 12. Cooling rates as a function of temperature for a primordial gas composed of atomic hydrogen and helium, as well as molecular hydrogen, in the absence of any external radiation. We assume a hydrogen number density $n_H = 0.045 \text{ cm}^{-3}$, corresponding to the mean density of virialized halos at $z = 10$. The plotted quantity Λ/n_H^2 is roughly independent of density (unless $n_H \gg 10 \text{ cm}^{-3}$), where Λ is the volume cooling rate (in erg/sec/cm^3). The solid line shows the cooling curve for an atomic gas, with the characteristic peaks due to collisional excitation of H I and He II. The dashed line (calculated using the code of Abel available at <http://logy.harvard.edu/label/PCas/cool.html>) shows the additional contribution of molecular cooling, assuming a molecular abundance equal to 0.1% of n_H .

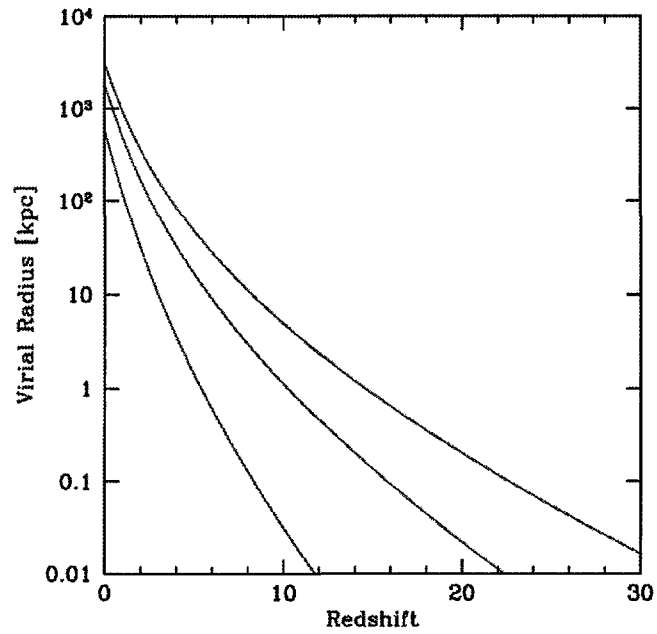


Fig. 7. Characteristic properties of collapsing halos: Halo virial radius. The curves show the virial radius of collapsing halos which correspond to $1 - \sigma$, $2 - \sigma$, and $3 - \sigma$ fluctuations (in order from bottom to top).

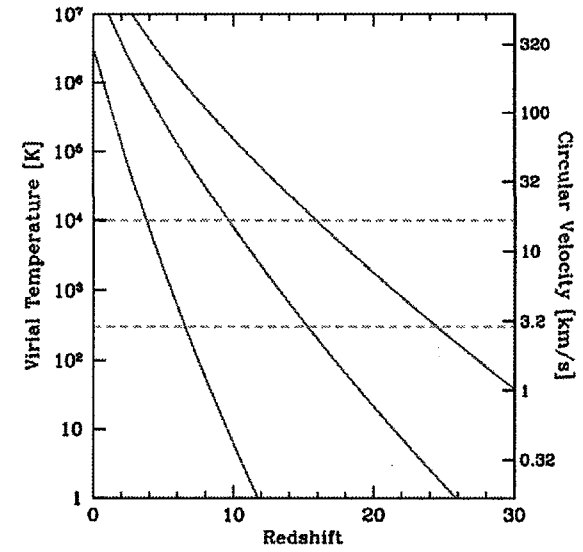


Fig. 8. Characteristic properties of collapsing halos: Halo virial temperature and circular velocity. The solid curves show the virial temperature (or, equivalently, the circular velocity) of collapsing halos which correspond to $1 - \sigma$, $2 - \sigma$, and $3 - \sigma$ fluctuations (in order from bottom to top). The dashed curves show the minimum temperature required for efficient cooling with primordial atomic species only (upper curve) or with the addition of molecular hydrogen (lower curve).

